23 Nonspherical Particle Measurements: Shape Factors, Fractals, and Fibers

PAUL A. BARON

Centers for Disease Control and Prevention,* National Institute for Occupational Safety and Health, Cincinnati, OH

CHRISTOPHER M. SORENSEN

Department of Physics and Program for Complex Fluid Flows, Kansas State University, Manhattan, KS

JOHN E. BROCKMANN

Sandia National Laboratories,† Albuquerque, NM

INTRODUCTION

Many aerosol measurement techniques are based on the behavior of ideal aerosol particles, that is, spherical particles with a density close to $1000\,kg/m^3$ [$1\,g/cm^3$]. In dealing with most real-world particles, allowances must be made for nonspherical particle behavior and other characteristics. In many situations, nonideal particle behavior can be considered as a modification of ideal particle behavior by using a correction factor, commonly called the *shape factor*. Two types of particles, agglomerates (or clusters of particles) and fibers, have been dealt with extensively in the literature and are discussed in more detail in this chapter. As well as being important for predicting particle behavior, particle shape can provide clues to the particle formation mechanisms.

SHAPE FACTOR

The dynamic shape factor relates the drag on an irregular particle to the drag on a sphere with the same particle mass and composed of the same material. The dynamic shape factor facilitates the transformation between the mass (or volume) equivalent diameter and the aerodynamic equivalent diameter of nonspherical and agglomerated particles (Brockmann and Rader, 1990). This transformation is necessary in aerosol dynamics codes (Gelbard, 1982), which describe the aerodynamic behavior of aerosol particle distributions while conserving mass. Helton et al. (1986) have shown that the results of aerosol behavior calculations can

*Mention of product or company name does not constitute endorsement by the Centers for Disease Control and Prevention.

†Sandia is a multiprogram laboratory operated by Sandia Corporation, a Lockheed Martin Company, for the United States Department of Energy under contract DE-AC04-94AL85000.

Aerosol Measurement: Principles, Techniques, and Applications, Second Edition, Edited by Paul A. Baron and Klaus Willeke.
ISBN 0-471-35636-0 Copyright © 2001 Wiley-InterScience, Inc.

be highly sensitive to the dynamic shape factor. Brockmann (1985, 1987) reviewed the wide range of dynamic shape factors reported in the literature.

The dynamic shape factor, χ, is defined as the ratio of the drag force on a particle, F_D, to the drag force on that particle's mass equivalent sphere, F_{DM}, at the same velocity, V.

$$\chi = F_D / F_{DM} \tag{23–1}$$

The dynamic shape factor has been developed as a correction to Stokes law drag for nonspherical particles (Hinds, 1999), that is, a Stokes law drag ratio (Clift et al., 1978). This definition expresses the drag on a nonspherical particle in the Stokes law regime as

$$F_D = 3\pi\mu\chi d_m V / C(d_m) \tag{23–2}$$

where μ is gas absolute viscosity, V is gas velocity past the particle, d_m is mass equivalent diameter of the particle, and $C(d_m)$ is slip correction factor for the mass equivalent diameter.

The choice of particle diameter used in the expression for slip correction has been a subject of concern (Cheng et al., 1988). Here, the use of the same equivalent diameter in the argument of the slip correction as is used in the expression for drag simplifies the presentation. This treatment will introduce a slight particle size dependence on dynamic shape factor in the transition regime. In the case of spherical nonporous particles, this treatment reduces to the correct usage.

Several equivalent particle diameters are defined in the literature. The mass equivalent diameter, d_m, of a particle is the diameter of a nonporous sphere composed of the bulk particle material that has the same mass as the particle. The envelope equivalent diameter, d_e, of a particle is the diameter of a sphere, which is composed of the bulk particle material and included void spaces (or voids), that has the same mass as the particle. When there are no included voids in the particle, these two diameters are identical. When there are included voids in the particle, these two diameters are different and $d_e > d_m$. The mobility equivalent diameter, d_B, of a particle is the diameter of a sphere with the same dynamic mobility as the particle. The aerodynamic equivalent diameter, or aerodynamic diameter, d_{ae}, of a particle is the diameter of a sphere of unit specific gravity that settles at the same terminal velocity as the particle.

These equivalent diameters are related by the dynamic shape factor χ, the particle material density ρ_p, and the unit specific gravity density $\rho_0 = 1000\,\text{g/m}^3$ [$1\,\text{gm/cm}^3$], and by the effective particle density ρ_e of a particle containing voids.

$$d_{ae}^2 \rho_0 C(d_{ae}) = d_m^2 \rho_p C(d_m) / \chi \tag{23–3}$$

$$d_B / C(d_B) = d_m \chi / C(d_m) \tag{23–4}$$

$$\rho_e d_e^3 = \rho_p d_m^3 \tag{23–5}$$

When the dynamic shape factor is defined with the particle material bulk density, it is comprised of two components:

$$\chi = \kappa\delta C(d_m) / C(\delta d_m) \tag{23–6}$$

The first component κ is due solely to the shape of the particle envelope (Fuchs, 1964). For oblate and prolate spheroids (Fuchs, 1964) and rectangular prisms (Johnson et al., 1987), κ may be calculated. These calculated values compare well with experimentally determined values (Johnson et al., 1987). The second component δ is due to particle porosity. This second

component is defined in terms of the particle bulk material density and the particle effective density as

$$\delta = (\rho_p/\rho_e)^{1/3} \tag{23–7}$$

The void fraction of a particle can be defined as $(1 - 1/\delta^3)$, and the envelope and mass equivalent diameters are related as

$$d_e = \delta d_m \tag{23–8}$$

Both κ and δ are potentially important for aggregate or agglomerate particles. Agglomerate particles with two basic morphologies are seen in the data of Kops et al. (1975), van de Vate et al. (1980), Allen and Briant (1978), Allen et al. (1978, 1979), Kasper and Shaw (1983), and Stöber et al. (1970). These morphologies are (1) a branched chain structure and (2) a compact aggregate with a more discernible enveloping shape. The dynamic shape factors of each of these two morphologies are also distinct. For the branched chain aggregates, the dynamic shape factor increases with the addition of primary spheres to the aggregate and is directly proportional to the cube root of the total number of primary particles (Stöber, 1971; Kops et al., 1975; Allen and Briant, 1978; Allen et al., 1979). This behavior is consistent with particles' shape determining their dynamic shape factor.

In compact agglomerates, the porosity component dominates the dynamic shape factor. Gieseke et al. (1977) define this component as the dynamic shape factor and employ it to characterize sodium oxide aerosols. The porosity component is also employed by Wegrzyn and Shaw (1979). For compact agglomerates, the shape factor is relatively independent of the number of primary particles but depends rather on the packing density of the primary particles in the aggregate (Kops et al., 1975; van de Vate et al., 1980). This behavior is consistent with the porosity of the agglomerate determining its dynamic shape factor.

FRACTAL PARTICLES

Introduction

Fractals are scale invariant objects. This means that they have dilation symmetry, that is, they look the same on all scales. Mathematical examples include the Koch curve, which has bumps upon bumps upon bumps, or the Sierpinski gasket, which has a descending series of holes, or the "dog chow" symbol shown in Figure 23–1, which has some similarity to the aggregates to be described here. Mathematical fractals are scale invariant over all scales, yet Nature provides many examples of objects that are fractals over a finite range of scales. Examples include coastlines that display inlets and peninsulas on a large scale (e.g., the western coastline of the island of Great Britain) and similar bumps and wiggles at much finer scale (e.g., a local map of a few miles of coastline). This scale invariance is not present in simple geometric objects. Thus, changing the scale of a circle makes it flatter or rounder; similarly, a square's corners get farther or closer apart. Fractal and geometric objects differ in another very important manner and that is in their dimensionality, a quantifiable parameter. Geometric objects have integer dimensions, while fractals have noninteger, fractal dimensions, D_f. An excellent introductory description of fractals is given by Family (1991).

The mathematical background of fractals and their relevance to natural objects put forward by Mandelbrot (1977, 1983) allowed Forrest and Witten (1979) to experimentally establish that random aggregates of metal smoke particles over a finite range of scales were fractals with a noninteger dimension. This seminal work caused an explosion of subsequent interest involving both simulation of aggregation mechanisms and experimental work on

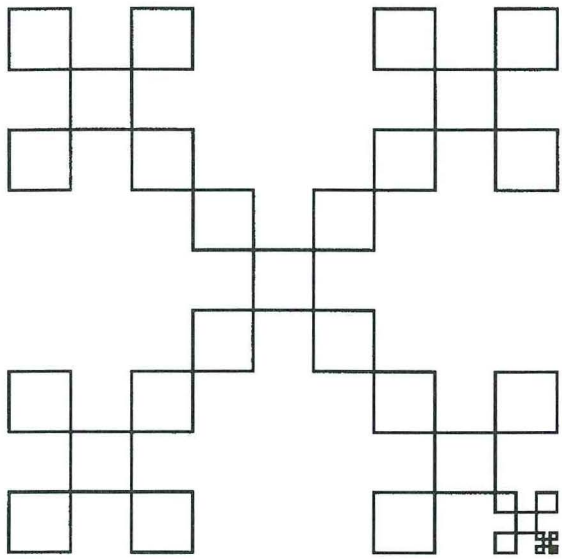

Fig. 23–1. "Dog chow" fractal with $D_f = \ln 5/\ln 3 = 1.465\ldots$. The pattern of five boxes in a larger box with three times the side length continues to all scales as implied by the box in the lower right.

aggregation in colloids and aerosols that continues today. The purpose of this chapter is to describe methods whereby the size and morphological parameters of fractal aggregates (i.e., aggregates composed of simple particles that display a fractal morphology) can be determined.

Fractal Aggregates

A fractal aggregate is an aggregate or cluster of particles that displays fractal scaling over the length scales from the primary or monomer particle size to the overall size of the aggregate. Fractal aggregates occur in aerosols and colloids as a result of random aggregation. Examples of both soot and titania fractal aggregates are given in Figures 23–2 and 23–3. The motion can be diffusive, ballistic (straight line), or in the crossover between these, and the resulting aggregate will be a fractal within the scale limits monomer to overall aggregate size. Both computer simulation and experiments have been important in establishing our knowledge of fractal aggregates (Family and Landau, 1984; Meakin, 1988; Viscek, 1992) because aggregation can be readily simulated on the computer. An example of a computer-generated fractal aggregate is given in Figure 23–4, and the similarity to the real-world examples given in Figures 23–2 and 23–3 is apparent. We now know that the aggregates can be classified into two major categories:

1. Particle-cluster aggregation, or diffusion-limited aggregation (DLA), which occurs when single monomers diffuse to and stick to a stationary, growing cluster (Witten and Sander, 1981). In three dimensions the clusters that result have a fractal dimension of $D_f \simeq 2.5$. It has recently been shown that those aggregates are not fractal over the entire range of their length scales (Oh and Sorensen, 1998).
2. Cluster–cluster aggregation, or diffusion-limited cluster aggregation (DLCA or DLCCA), which occurs when all clusters diffuse and then stick when they randomly touch (Kolb et al., 1983; Meakin, 1983). In three dimensions the clusters that result have a fractal dimension of $D_f \approx 1.75$ when the cluster motion is diffusive. Ballistic motion

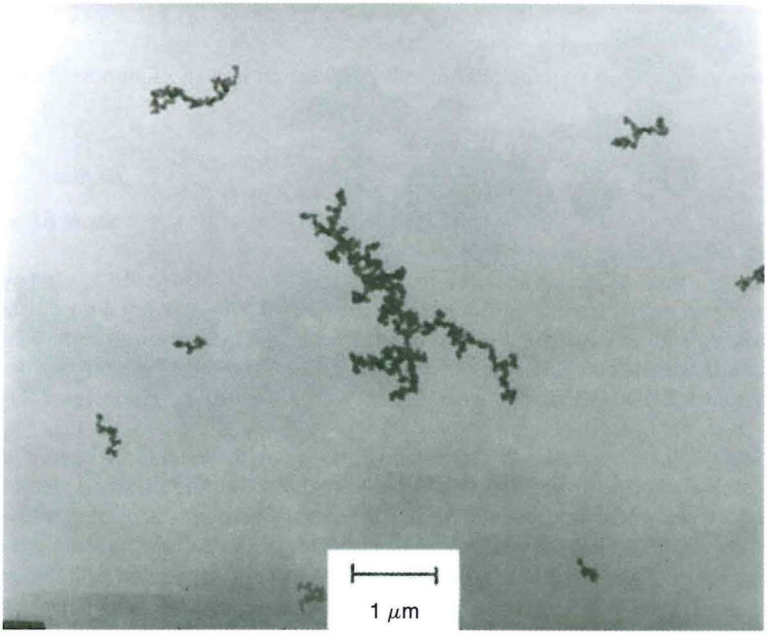

Fig. 23–2. Soot fractal aggregates from a premixed methane flame. The fractal dimension is $D_f \approx 1.8$.

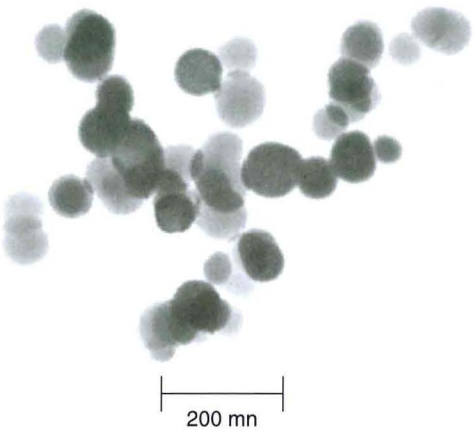

Fig. 23–3. TEM picture of titania (TiO_2) fractal aggregates with $D_f \approx 1.8$ produced by pyrolysis of titanium isopropoxide.

causes $D_f \approx 1.9$ (Meakin, 1984). If the sticking probability is significantly less than one, the reaction-limited cluster aggregation (RLCA) regime is entered for which $D_f \approx 2.15$, a situation important for many colloids (Lin et al., 1990). It is now known that only cluster–cluster aggregates occur in aerosols and colloids, with the DLA morphology finding application in other areas.

The meaning of the fractal dimension is in the relation between linear and volumetric size, the latter of which is linearly related to the mass or number of primary particles per aggre-

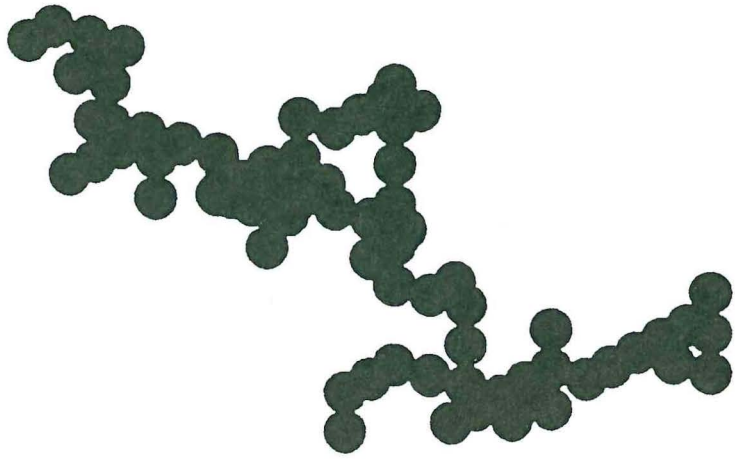

Fig. 23–4. A simulated DLCA aggregate with $D_f = 1.79$.

gate N. If R is a linear size of the aggregate, then $N \propto R^{D_f}$. We say that "the mass" N scales with linear size to the fractal dimension D_f. Geometric objects scale as well; for example, the volume of a sphere increases by a factor of eight when the diameter is doubled because its dimensionality is three, but fractals have a noninteger dimension D_f less than the embedding spatial dimension d, that is, $D_f < d$.

The beauty of the fractal dimension is that it allows a quantitative description of the degree of openness, or ramification, of the random aggregate. The smaller the D_f relative to the spatial dimension d, the more quickly the aggregate fills space as R increases. The fractal dimension plays a part in determining the aggregate density, the optical properties, the way in which it diffuses, and the kinetics of its further growth.

The relation between "mass" and linear size for a fractal aggregate can be quantified in three ways, all of which will form a basis for measurement of D_f to be describe below. We let a be the monomer (primary particle) radius and R_g be the radius of gyration (a root mean square radius; see below) of the aggregate. Then

$$N = k_o(R_g/a)^{D_f} \tag{23–9}$$

In Eq. 23–9 k_o is a constant of order unity (Wu and Friedlander, 1993), perhaps best described by $k_o \approx 1.3$ to 1.4 (Cai et al., 1995a; Oh and Sorensen, 1997; Sorensen, 1997) but see also Köylü and Faeth (1992). This is perhaps the most important defining relation for a practical description of a fractal aggregate. Another important relation describes the spatial correlation function of the density $g(r)$ given by

$$g(r) \approx r^{D_f - d} h(r/\xi) \tag{23–10}$$

where $g(r)$ is a conditional probability relating on average the density at two points separated by a distance r. The function $h(x)$ is a cut-off function for the power law, $h(x < 1) \approx 1$, but $h(x)$ decreases more rapidly than any power law for $x > 1$. This implies that the length ξ is on the order of the size of the aggregate. For DLCA the Gaussian $h(x) \approx \exp(-x^2)$ is fairly accurate (Sorensen et al., 1992b; Cai et al., 1995a; Sorensen and Wang, 1999). A third valuable relation involves the amount of material within regions of side length s centered on the aggregates. For a fractal particle

$$N \approx s^{D_f} \tag{23–11}$$

All three of these equations will be used for the particle analysis described below.

Real Space Analysis

Collection Methods

Thermophoretic Collection. Often aerosols are hot, for example, soot in a flame or metal oxides from a reactor, and insertion of a colder probe will cause thermophoresis of the hot aerosol particles down the thermal gradient to the colder probe. The great advantage of thermophoresis is that all particle sizes move at the same rate; hence the sampling is unbiased (Rosner et al., 1991) (at least for submicrometer particles; see Sorensen and Feke, 1996).

A "frog tongue" probe device designed after Dobbins and Megaridis (1987) has been used to sample flame soot and TiO_2 and SiO_2 aerosols with apparent success (Cai et al., 1993). This device was built from a modified disk hard drive and a carbon arrow shaft. The essential quality is the ability to inject quickly a probe into the aerosol, hold it there for a residence time determined by the operator, and then quickly remove the probe. The device can move the probe 5 cm in 3 ms and has a selectable residence time of 15 to 150 ms.

The "frog tongue" part of the probe is a thin "knife-blade" of metal. Transmission electron microscope (TEM) copper grids are mounted on the blade with polystyrene cement. This cement is easily broken so that the grid can be removed. The grids consist of copper mesh, having either a carbon or a Formvar coating. The blade is inserted with its face parallel to the aerosol flow to avoid perturbation of the flow and impaction of particles.

Impaction Collection. Placing a probe with its face perpendicular to the aerosol flow will allow impaction of aggregates onto the probe. This approach was used to collect soot particles 1 μm sized or larger (Sorensen and Feke, 1996; Sorensen et al., 1998). Impaction relies on inertia, so there is a bias toward collecting a larger fraction of the bigger aggregates. The Stokes number quantifies the likelihood of impaction and is discussed in Chapters 4 and 10.

Collection by Settling. Often the aerosol settles out to form a powder at the bottom or on the sides of the chamber, container, room, or region of aerosol study. This powder can be carefully collected and redispersed to create samples for microscopic examination. Collection should proceed with some care because the fractals may be fragile, as implied by their tenuous nature. Little is known about the fragility of fractal aggregates. Experiments exist in which aggregates have been stretched and then snapped back (Friedlander et al., 1998). These imply considerable resiliency. Despite this, any reasonable caution when handling would not be wasted.

Redispersion has been accomplished using volatile liquids, perhaps with surfactants, and then drying. Water, ethanol, and acetone have been used to study carbonaceous soot and TiO_2. Water has a large surface tension, and this tends to crush the aggregate as it dries. Aerosol methods have been used for redispersion of soot (Prenni et al., 2000), though it has not been established that individual particles retain their original structure. Each type of material has its own peculiarities, so experimentation is warranted.

In all cases collection densities on the microscope substrate (e.g., TEM grid) should not be great, the aggregates occupying 10% of the area or less (Cai et al., 1993). This is necessary to avoid significant "artificial" aggregations on the substrate. If two aggregates overlap

on the substrate, there is no way to distinguish the resulting cluster from one that formed in the aerosol phase.

Analysis of Projected Images

Visualization. An electron microscope is necessary to study nearly all conceivable fractal aggregates because the primary particles (or monomers) are smaller than optical wavelengths ("big" particles do not stick together readily). Standard carbon- or Formvar-coated copper grids are sufficient to hold the sample. The magnification should be large enough to allow an accurate measurement of the monomer. For example, soot is usually composed of aggregates of monomers with radii $a \approx 10\,\text{nm}$. To magnify these to 1 mm images requires 100,000 magnification.

Photographs can be digitized with a digital scanner for computer analysis. The image data will be in the form of a two-dimensional array with a magnitude representing the gray level at a given pixel. A computer analysis routine can be written to identify individual clusters in the digitized array, or the operator can look at the image on the monitor, pick out the images visually, and store them as separate gray level arrays, one for each cluster. Often it is useful to subtract a background from this cluster gray level. The background is the average gray level of the pixels near the circumference of cluster. With this subtraction, all the nonaggregate pixels are set to zero ("white"). Once a gray level array for each cluster is achieved, analysis for morphological parameters can begin.

A major problem in the analysis of the cluster morphology is that the three-dimensional structures are viewed as two-dimensional projections as a consequence of the microphotography. One way to overcome this is to view the clusters in at least two different projections and with this stereo technique regenerate the true three-dimensional structure. This has been done in the past (Sampson et al., 1987; Köylü et al., 1995) but the method is laborious and, as will be shown, largely unnecessary. If the analysis is limited to one projection, and if the density of this projection can give accurate information regarding the total mass along a given projection through the cluster, then a viable analysis of the three-dimensional morphology can be obtained. Such a mass-preserving image is difficult to achieve, however, because the attenuation of the electrons producing the projected image is not linearly related to the total mass of material through which the electrons passed. Furthermore, the response of the photographic film that captures the image is linear only over a small range before it saturates and becomes insensitive to the mass of the cluster above it. In previous work involving small soot clusters (Cai et al., 1993), some success was achieved with mass-preserving projections largely because the clusters were small enough to keep the gray level–to–projected mass relationship approximately linear. In general, however, mass-preserving projection is uncertain, so we are left with projection of the cluster onto the two-dimensional plane in a binary format, that is, a shadow, in which any part of the cluster is the same degree of gray (black) as any other and the background is white. The advantage of this method is that it eliminates the response of the detector. The *conversion to a binary format appears not only easier to apply, but also more reliable and accurate.* What is needed is a quantitative method to convert two-dimensional information into three-dimensional information, and such a method is presented below. The bulk of the discussion applies to DLCA aggregates with $D_f \approx 1.75$, which are very typical. When $D_f > 2$, the problem of determining the size parameters of aggregates is much less explored, but a possible direction will be suggested.

Binary Projection Analysis

THE RADIUS OF GYRATION. We first consider the radius of gyration R_g of a three-dimensional body as given by

$$R_g^2 = \frac{\int r^2 \rho(r) d^3 r}{\int \rho(r) d^3 r} \tag{23–12}$$

where $\rho(r)$ is the density. A reasonable assumption is made that an ensemble of clusters on a TEM grid when viewed from one direction will yield an average spherical symmetry. Then, because $r^2 = x^2 + y^2 + z^2$, and because a projection onto a plane eliminates one of the dimensions, it follows from Eq. 23–12 that (Cai et al., 1993)

$$R_{g,3} = \sqrt{3/2} R_{g,proj} \tag{23–13}$$

In Eq. 23–13, $R_{g,3}$ is the true, three-dimensional radius of gyration of the cluster and $R_{g,proj}$ is that observed for the mass-preserving projected image. The factor 3/2 results from the elimination of one of the three dimensions. Furthermore, Eq. 23–13 applies to a mass-preserving projection. Equation 23–13 is verified by the computer simulations of Köylü et al. (1995), who found the empirical factor relating the two radii to be 1.24 ± 0.01, in good agreement with $\sqrt{3/2} = 1.225$.

The previous discussion shows the difficulty in achieving an accurate mass-preserving projection, so Eq. 23–13, while informative, is of questionable utility. The purpose here is to show that a better measurement can be obtained with a two-dimensional binary representation of the cluster. It is well established that the fractal dimension of $d = 3$ DLCA clusters is less than 2; typically, D_f is in the range 1.7 to 1.8. Thus, it might be expected that the image of a cluster projected onto a plane in a binary format would be mass preserving (i.e., no significant screening or occultation between monomers would occur). This would imply that the number of monomers in the aggregate would be proportional to the projected area of the cluster (i.e., $N \propto A_c$). It must be stressed that this expectation is only correct for asymptotically large ($N \to \infty$) clusters. For finite size clusters, however, screening occurs, and it is found empirically that

$$N = A_c^{\alpha} \tag{23–14}$$

where $\alpha = 1.1$ (for references and a complete discussion, see "Determination of N," below). Thus, the effective fractal dimension in the two-dimensional plane of the binary projection should be different from the fractal dimension of the real, three-dimensional cluster. In the immediately following argument, we will call these fractal dimensions $D_{f,2}$ and $D_{f,3}$, respectively.

Consider how the three-dimensional cluster is projected onto the two-dimensional plane. With spherical or circular symmetry, we assume the density profile of either the three-dimensional fractal cluster or its projection is given by

$$\rho(r) \propto r^{D_f - d} \quad \text{for } r \le R \tag{23–15a}$$

$$= 0 \quad \text{for } r > R \tag{23–15b}$$

where R is the perimeter radius and $D_f = D_{f,2}$ or $D_{f,3}$, depending on the spatial dimension of $d = 2$ or 3 for the binary projected or real cluster, respectively. Then Eq. 23–12 yields

$$R_{g,3}^2 = \frac{D_{f,3}}{D_{f,3} + 2} R^2 \tag{23–16}$$

$$R_{g,binary}^2 = \frac{D_{f,2}}{D_{f,2} + 2} R^2 \tag{23–17}$$

Thus, a relation between the true radius of gyration $R_{g,3}$ and the measured, binary projection radius of gyration $R_{g,binary}$ can be determined if we have a relation between $D_{f,3}$ and $D_{f,2}$.

To determine this latter relation, consider the empirical fact of Eq. 23–14 that $N_3 \approx A_c^{\alpha}$, where we now label the number of monomers per cluster with a subscript of three to designate that this is the number in three-dimensional space (i.e., the true number). We also have by Eq. 23–9 the relation $N_3 \approx R_{g,3}^{D_{f3}}$. The binary projection has analogous relations such that $N_2 \approx R_{g,binary}^{D_{f2}}$, which defines $D_{f,2}$, but, and here is the key, $N_2 \approx A_c$. Furthermore, by Eqs. 23–16 and 23–17, $R_{g,3} \approx R_{g,binary}$. All these proportionalities together yield

$$D_{f,2} = D_{f,3}/\alpha \tag{23–18}$$

This result is consistent with past work that has measured the fractal dimension of clusters in terms of both three-dimensional quantities and projectional quantities, where it was found that the projectional dimension is typically 10% less than that determined with the three-dimensional quantities (Sampson et al., 1987; Zhang et al., 1988; Cai et al., 1993). It is also consistent with simulations by Jullien et al. (1994), who also found the projectional fractal dimension to be about 10% less than the fractal dimension of the unprojected clusters. Because $\alpha \approx 1.1$, we believe Eq. 23–18 explains these past observations. Finally, we use Eqs. 23–16 to 23–18 to find

$$R_{g,3} = \left(\frac{D_{f,3} + 2\alpha}{D_{f,3} + 2}\right)^{1/2} R_{g,binary} \tag{23–19}$$

Now recall that $R_g \equiv R_{g,3}$ and $D_f \equiv D_{f,3}$. Then for typical values of $D_f = 1.8$ and $\alpha \approx 1.1$, this correction factor is 1.026. Thus, as anticipated and qualitatively explained earlier (Cai et al., 1993), the binary projection yields a remarkably accurate measure of the true, three-dimensional radius of gyration.

Computer analysis of the clusters begins with the total gray level defined as

$$G_{tot} = \sum_{x,y} G(x,y) \tag{23–20}$$

where $G(x,y) = 0$ or 1 is the gray level of the pixel at position (x,y). Because $G(x,y)$ is binary, G_{tot} is the total number of pixels in a cluster. To determine the radius of gyration R_g of a cluster, first calculate the cluster center of mass:

$$\vec{r} = G_{tot}^{-1} \sum_{x,y} G(x,y)\vec{r}(x,y) \tag{23–21}$$

and then the radius of gyration

$$R_{g,binary}^2 = G_{tot}^{-1} \sum_{x,y} G(x,y)[\vec{r}(x,y) - \vec{r}_{cm}]^2 \tag{23–22}$$

Correction using Eq. 23–19 to obtain $R_g/R_{g,3}$ could now be made, but because the correction is only about 2%, this is hardly warranted given that other experimental errors are most likely larger.

Another useful, and fairly simple, method to determine R_g is using the maximum, projected length of the aggregate image. Computer simulations indicate that half this length (hence a radius) R_2 is a constant ratio to R_g independent of N. This is shown in Figure 23–5. The result is that

$$R_g/R_2 = 0.69 \pm 0.03 \tag{23–23}$$

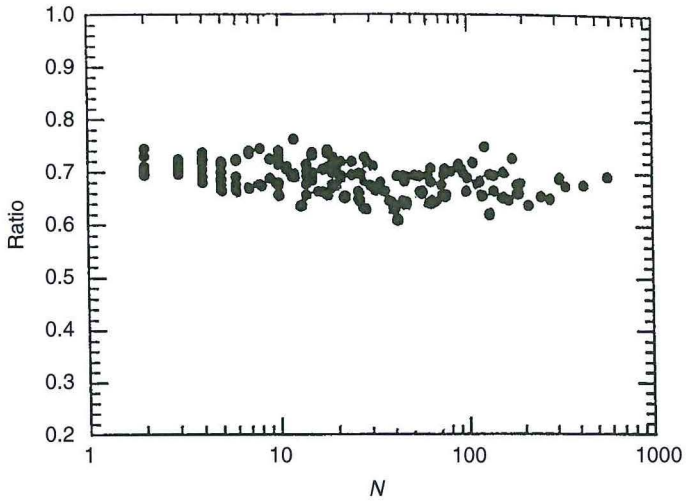

Fig. 23–5. Ratio of the aggregate radius of gyration R_g (in $d = 3$ space) to half the longest length R_2 of the clusters projected onto a $d = 2$ plane as a function of N for simulated DLCA aggregates with $D_f = 1.79$.

This method is simpler than calculation of R_g from the gray level, Eq. 23–22, but relies on the clusters being DLCA with $D_f \approx 1.79$ (i.e., equivalent to the simulation that produced Fig. 23–5).

DETERMINATION OF N. Determination of the number of monomers per aggregate N from the projected area of a cluster has a long and well established history for DLCA ($D_f \approx 1.75$) (Medalia, 1967; Medalia and Heckman, 1969; Mandelbrot, 1977; Sampson et al., 1987; Megaridis and Dobbins, 1990; Köylü and Faeth, 1992; Cai et al., 1993; Köylü et al., 1995). In general it is found that

$$N = k_a (A_c / A_p)^{\alpha} \tag{23–24}$$

where k_a and α are constants near unity and A_c and A_p are the projected areas of the cluster (aggregate) and primary particle (monomer), respectively. Medalia and Heckman (Medalia, 1967; Medalia and Heckman, 1969) first used this form and found empirically $k_a = 1.0$ and $\alpha = 1.1$. This has subsequently been corroborated by a number of workers with α varying by a few hundredths. Sorensen and co-workers (Oh and Sorensen, 1997) found that fractal soot clusters with $D_f \approx 1.75$ obeyed Eq. 23–24 with $\alpha = 1.09$. Köylü et al. (1995) analyzed both computer-simulated and real soot clusters and found $k_a = 1.15 - 1.16$ and $\alpha = 1.09 - 1.10$. Note that with these results the limit as $N \to 1$ is not preserved because k_a is not unity. In another simulation, Meakin et al. (1989) created DLCA clusters with $D_f = 1.8$ and N up to $N = 10^4$, larger than any in any other work that has compared N to the projected area. They fit their data with

$$A_c / A_p = 0.4784 N + 0.5218 N^{0.7689} \tag{23–25}$$

This result is equivalent to Eq. 23–24 with $k_a = 1.00$ and $\alpha = 1.10$ over the range of $N = 1$ to 100, $k_a = 1.00$ and $\alpha = 1.084$ for $N = 1$ to 1000, $k_a = 1.075$ and $\alpha = 1.083$ for $N = 10$ to 100, and $k_a = 1.106$ and $\alpha = 1.069$ for $N = 10$ to 1000. The slope of a log N versus log (A_c/A_p) graph is α, and Eq. 23–25 yields a slowly decreasing α with increasing N. This is consistent with the

notion that, for clusters with $D_f < 2$, as $N \to \infty$, N should be linear with A_c, that is, α asymptotically approaches 1.00 because the cluster dimension is less than the dimension of the plane onto which it is projected.

In summary, all these results agree fairly well. Given this and because we desire to conclude with a recommendation for all plausible situations, we use the computer results of Meakin et al. (1989), Eq. 23–25, which are the most extensive (up to $N = 10^4$). A good procedure is to estimate the range of N values for the clusters to be analyzed and then fit Eq. 23–24 to Eq. 23–25 for this range to determine α and k_a. Then use these values to determine N from A_c and A_p. For example, if the clusters lie in the approximate range $N = 10$ to 1000, use $k_a = 1.106$ and $\alpha = 1.069$. Most likely other sources of experimental error will be larger than the uncertainty incurred by use of k_a and α.

THE FRACTAL DIMENSION. There are three useful ways to determine the fractal dimension D_f. Two methods analyze a single cluster; they are the method of nested circles or squares and the analysis of the density correlation function. The third method requires an ensemble of aggregates and compares N to R_g (or any measure of the aggregate's linear size) via Eq. 23–9. We discuss these methods sequentially below.

The Method of Nested Circles or Squares. In this method circles or squares of increasing radius or side length s are computer drawn on the aggregate centered on the aggregate's center of mass. The total binary black area within the circle or square is calculated and plotted versus s. Then from Eq. 23–11 the following scaling relation holds:

$$D \approx s^{D_{f2}} \tag{23–26}$$

Equation 23–26 is best used as a log–log plot of G versus s, which will have a slope of D_{f2}. D_{f2} must be converted to the three-dimensional fractal dimension with Eq. 23–18 and α.

Often a given cluster will yield a nonlinear, strangely shaped plot of N versus s. One must remember that "fractal" is a statistical concept, and not all clusters are alike. Examination of an ensemble of clusters is therefore highly recommended. While most clusters will exhibit fractal behavior, that is, have a linear $\log G$ versus $\log s$ plot, occasional "odd" clusters will occur. An example of this cluster-to-cluster variation is given by Zhang et al. (1988) and reproduced in Figure 23–6. There it is found that the sum of the black areas for three clusters is better described by Eq. 23–26 than for any individual cluster. On the other hand, if there are more "odd" clusters than "fractals," then the system is not a fractal system.

The Density Correlation Method. The density correlation function is a conditional probability that, given material at one point, defines the probability that there will be material at another. It is represented by $g(r)$ and is expressed by

$$g(r) = [\rho(R+r)\rho(R)] \tag{23–27}$$

In Eq. 23–27 $\rho(R)$ is the density at point R, and the brackets mean an average over all positions R.

The digitized, binary images can be used to calculate $g(r)$. Because the density is proportional to the gray level of the image, Eq. 23–20, we can write

$$g(r) = \sum_{u}^{N_u} \sum_{v}^{N_v} D(u+x)D(v+y)/N_u N_v \tag{23–28}$$

where

$$r = \sqrt{x^2 + y^2} \tag{23–29}$$

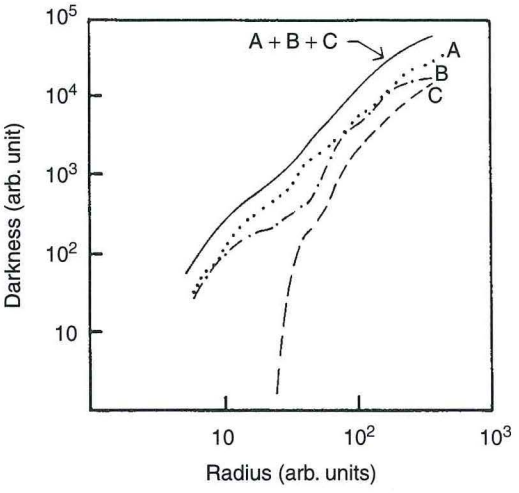

Fig. 23–6. The total gray level (G_{tot}) within a series of nested circles centered on the cluster center of mass for three different soot clusters A, B, and C determined from their binary projected images. The curve $A + B + C$ is their sum, which is fairly linear to imply an average $D_f = 1.72 \pm 0.10$.

In calculating with Eq. 23–28, u and v should be constrained to points (pixels) within the aggregate. This is not necessary, but otherwise $G = 0$ and unnecessary computation results. Note that Eq. 23–28 could also be restricted to averages over u or v separately to yield $g(x)$ and $g(y)$. If these differed, anisotropy would be implied. Many different x and y values yield the same r, so these could be averaged over a range r to $r + dr$ to calculate a final $g(r)$.

Once the density correlation function is calculated, it can also be plotted on a log–log plot to display its power-law nature, as written in Eq. 23–10. If the projected image has been stored in the computer in a binary format, the projected image has pixels with gray level $G = 0$ or 1 only, and the effective spatial dimension is $d = 2$ to be used in Eq. 23–10. Also for the binary format, the fractal dimension is $D_{f,2} = D_{f,3}/\alpha$ (i.e., the correction of Eq. 23–18 must be made). Here again cluster-to-cluster variation is expected, but typically not as much as in the "nested" method above. Figure 23–7 gives an example for a soot fractal aggregate.

The Ensemble Method. Both N and R_g can be extracted from the projected, binary images of the fractal aggregates. Given these parameters, Eq. 23–9 suggests that a log–log plot for a polydisperse ensemble of aggregates will yield D_f from the slope and k_o from the intercept. This fact has been used many times in the literature, and Figure 23–8 gives an example. Note that this analysis yields $D_f \equiv D_{f,3}$.

If k_o is not needed, this analysis can be simplified by using the total gray level of the binary projected image of the aggregate versus any aggregate length (e.g., the longest, $2d$ projected length). The slope of such a graph would yield $D_{f,2}$. This method usually yields excellent results.

Aggregates with $D_f > 2$. Jullien et al. (1994) modeled $d = 3$ random fractal aggregates on a computer with $1 \leq D_f \leq 2.5$ and then studied their projection onto a plane. Figure 23–9 is a reproduction of their Figure 2a, which is particularly useful. It shows the binary projected fractal dimension $D_{f,2}$ versus the true $d = 3$ fractal dimension D_f of the aggregate for a variety of aggregate sizes ranging from $N = 16$ to 8192. A line representing Eq. 23–18 with $\alpha = 1.1$ is included. The data for $D_f < 2$ support the line, giving yet more credence to the analysis above. For $D_f > 2$, this line fails, more so with increasing D_f. However, larger values of α in Eq. 23–18

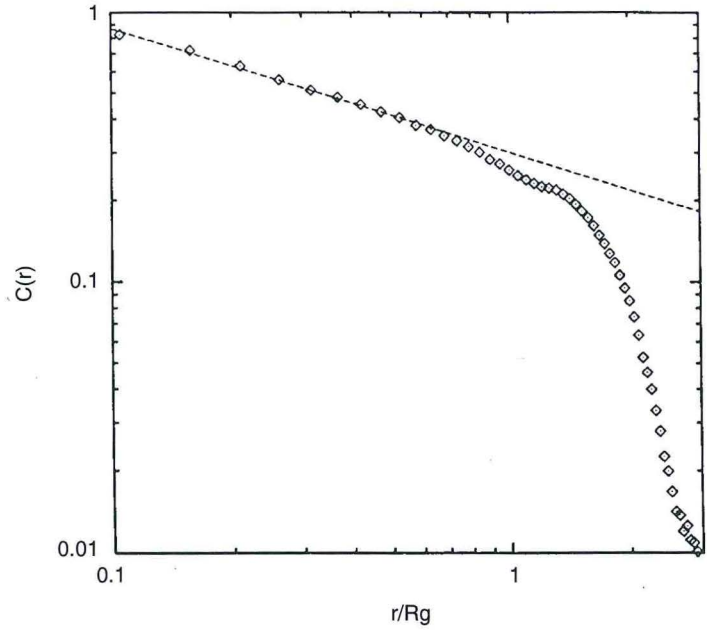

Fig. 23–7. Density correlation function for a soot cluster obtained from a premixed CH_4/O_2 flame. Dashed line is a fit to the first 13 points (thereafter the cut-off function $h[x]$ takes over) of the power law $g(r) \approx r^{D_{f,2}-d}$.

could describe the relationship between D_{f2} and $D_f > 2$. Given this, if one need analyze an aggregate with $D_f > 2$, α can be extracted from Figure 23–9, and then the analysis technique described above using Eqs. 23–18, 23–19, and 23–24 can be applied.

Optical Characterization of Fractal Aggregates

Light scattering is an excellent method for in situ determination of fractal aggregate size and morphology (Sorensen, 1997, 2001; Oh and Sorensen, 1999). The method involves measuring the scattered intensity I as a function of the scattering wave vector q, where

$$q = 4\pi\lambda^{-1}\sin(\theta/2) \tag{23–30}$$

λ is the optical wavelength, and θ is the scattering angle. Although θ is the experimental parameter, it is important to both think and work in terms of q because inverse q is the length scale of the scattering experiment. Plots of I versus q will have changes of slope whenever q^{-1} passes through a length scale change of the system. I versus q is called the *optical structure factor*. Figure 23–10 is a schematic diagram of the information that can be obtained from an optical structure factor measurement. At small q the scattering is constant and proportional to the cluster number density n and the number of monomers per cluster N squared. This is termed the *Rayleigh regime*. Note that in an aggegating system $nN = n_m$, the monomer number density, which is ideally a conserved quantity. Then $I \approx nN^2 = n_m N$, which will increase as the system aggregates because N increases. This increase in scattering (in the Rayleigh regime) as the system coarsens is the Tyndall effect (see Kerker, 1969) for a fractal aggregate system.

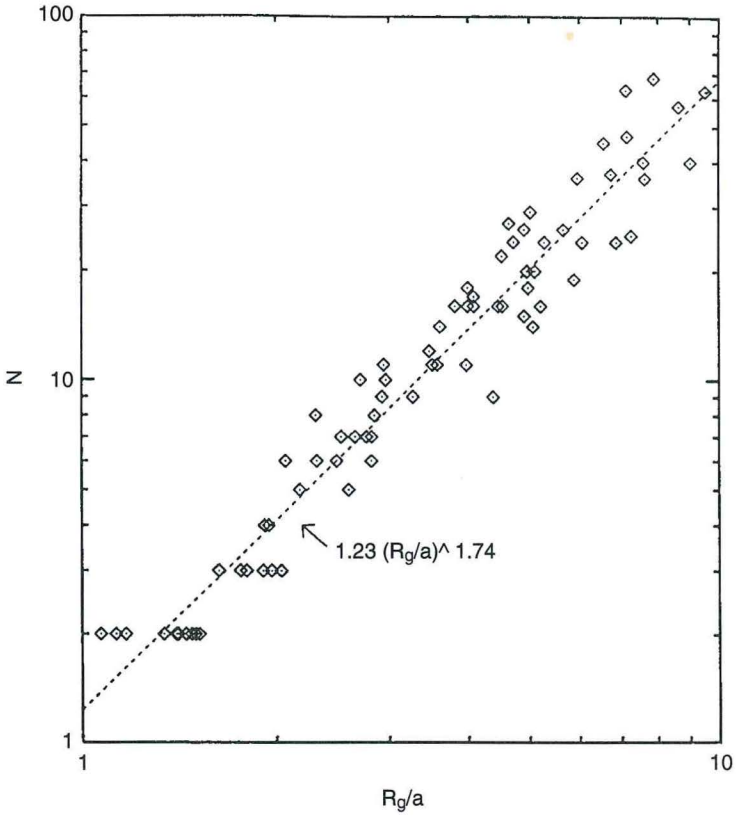

Fig. 23–8. Total number of monomers per aggregate versus radius of gyration divided by the monomer radius for an ensemble of soot clusters collected from a premixed methane/oxygen flame. The slope of this log–log plot demonstrates the power-law dependency of Eq. 23–1 and yields a fractal dimension of $D_f = 1.74 \pm 0.04$. The intercept yields $k_o = 1.23 \pm 0.07$.

As q increases from the Rayleigh regime, the slope eventually changes, indicating an aggregate length scale. Qualitatively one need only measure q where this first bend in I versus q occurs, invert it to q^{-1}, and identify this length as the overall average size of the aggregates. This can be quantified because this first bend is the Guinier regime where (Guinier et al., 1955)

$$I(q) = I(0)\left(1 - q^2 R_{g,z}^2/3\right) \tag{23–31}$$

In Eq. 23–31 $R_{g,z}$ is the z-average radius of gyration

$$R_{g,z}^2 = \int R_g^2(N) N^2 n(N)\,\mathrm{d}N \Big/ \int n(N)\,\mathrm{d}N \tag{23–32}$$

$n(N)$ is the number of aggregates of size N per unit volume (i.e., the aggregate size distribution). After the Guinier regime comes a regime of constant slope (on this log–log plot), the so-called power-law regime where (Sorensen and Wang, 1999)

$$I(q) = I(0) C_p C (q R_{g,z})^{-D_f} \tag{23–33}$$

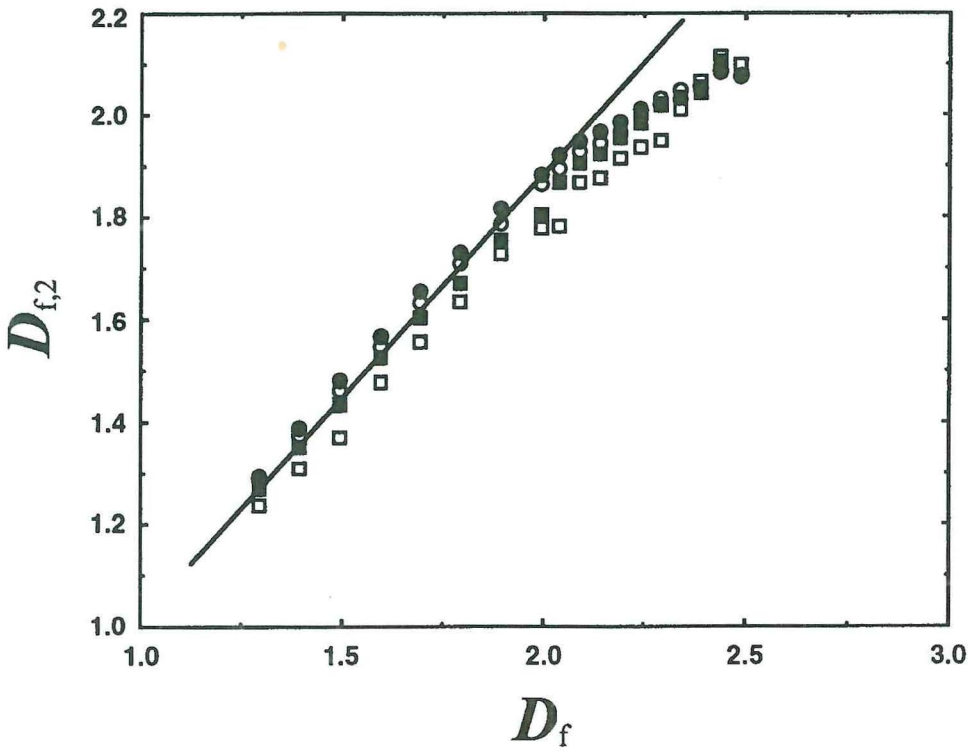

Fig. 23–9. Fractal dimension D_{f2} of the projection of a fractal aggregate versus its $d = 3$ space fractal dimension, D_f, for $N = 16$ (open circles), 128 (filled circles), 1024 (open squares), 8192 (filled circles) for computer-simulated aggregates after Jullien et al. (1994). Line is Eq. 23–10 with $\alpha = 1.1$.

In Eq. 23–33 C_p and C are constants to be described below. The important dependency is $I \propto q^{-D_f}$, which means that the slope of the double-log plot of I versus q is the negative fractal dimension; hence, D_f can be measured.

Finally, at highest q, another bend occurs indicating the monomer radius a. Thereafter, the monomer regime is entered with slope –4 (a Porod regime) if the monomers have a smooth, nonfractal surface.

Optical Structure Factor Measurements—Quantitative Description. With the qualitative description of the optical structure above, we now describe how to obtain accurate values of fractal aggregate R_g and D_f from light-scattering measurements.

Measurement of R_g. An example of an optical structure factor from some of our early work (Gangopadhyay et al., 1991) is given in Figure 23–11 for a soot aerosol in a premixed methane/oxygen flame. Aggregation increases with increasing height above the burner. Inspection of Figure 23–11 shows that with increasing height, the bend in the optical structure factor (i.e., where the slope of I versus q goes from zero to negative) progresses to smaller q. The cardinal rule is that a change in slope implies a length scale. In this case the length scale is the overall aggregate size, and because $R \approx q^{-1}$, this is a direct observation, albeit qualitative, of the aggregate size increasing with time. Notice the essentially isotropic scattering at $h = 8$ mm to indicate very small particles. Figure 23–12 presents a more recent example of scattering from a titania aerosol. Note the scale in q is an order of magnitude smaller than in Figure 23–11, and hence the clusters of titania are an order of magnitude larger. In Figure 23–12 a significant power-law regime is seen with a slope implying $D_f \approx 1.7$.

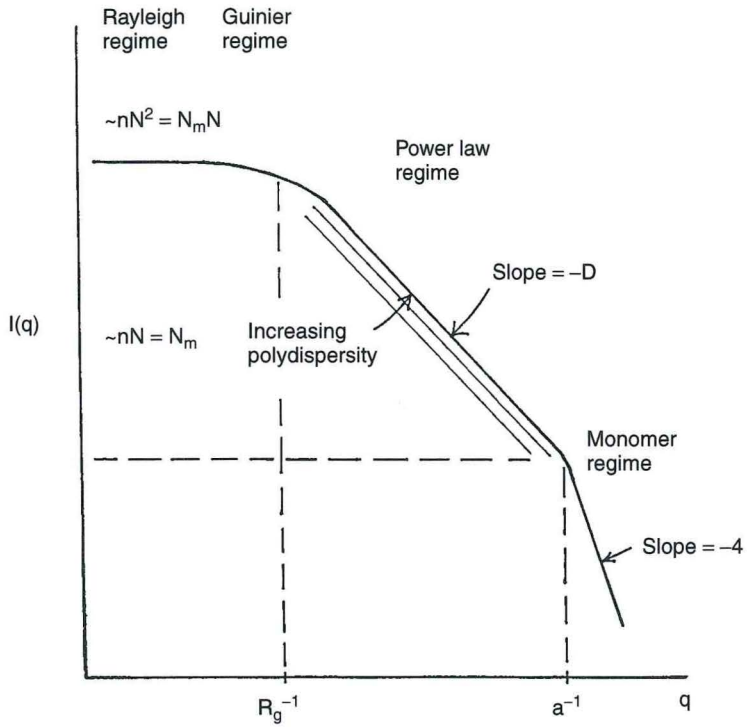

Fig. 23–10. Schematic representation of the scattered light intensity $I(q)$ versus $q = 4\pi\lambda^{-1}\sin\theta/2$, where θ is the scattering angle, from an ensemble of fractal aggregates of dimension D_f with N monomers per aggregate on a log–log plot. In the ensemble n is the number density of clusters and N_m is the total number of monomers, $nN = N_m$.

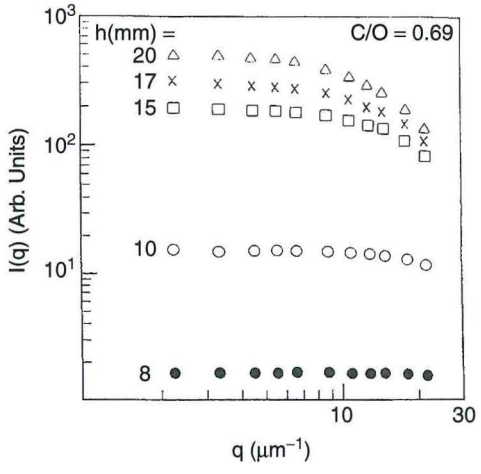

Fig. 23–11. Scattered light intensity $I(q)$ as a function of the scattering wave vector q for five different heights above burner h for a premixed methane/oxygen flame.

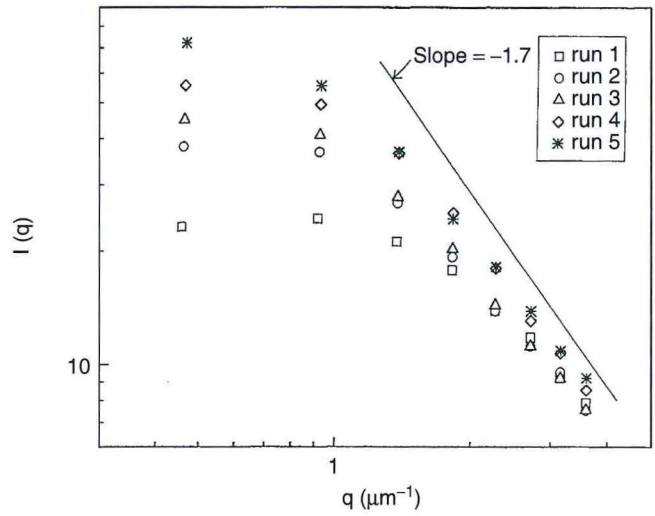

Fig. 23–12. Scattered light intensity $I(q)$ as a function of the scattering wave vector q for a titania aerosol.

Quantitative analysis of the optical structure factor proceeds in two steps (Sorensen et al., 1992a; Sorensen, 2001). First, the Guinier regime is analyzed to yield the aggregate radius of gyration. The Guinier equation, Eq. 23–31, may be inverted to yield

$$I(0)/I(q) \approx 1 + \frac{1}{3} R_{g,z}^2 q^2 \tag{23–34}$$

This implies that a graph of $I(0)/I(q)$ versus q^2 should be linear with a slope of 1/3 $R_{g,z}$. This plot is similar to the Zimm plot of biophysics (Zimm, 1948; Tanford, 1961; Kerker, 1969). The data of Figure 23–11 are so plotted in Figure 23–13. Figure 23–13 is a proper Guinier analysis in that, for the most part, for the data used, $qR_g < 1$, which is equivalent to $I(0)/I(q) < 4/3$. Precisely speaking, this Guinier analysis should be limited to $qR_g \leq 1$. Often, however, the data are not plentiful and precise enough within these bounds to yield an accurate R_g. It has been found (Cai et al., 1995b) through experience with both real data and numerical calculations to create simulated data, that $I(0)/I(q)$ versus q^2 remains linear well beyond these limits, and data up to about $I(0)/I(q) \approx 2$ can be trusted to yield accurate R_g values.

Measurement of D_f. The power-law regime yields the fractal dimension D_f by its slope. One would like to have a good decade of linearity to get a good measure of this slope but this is rarely the case. Moreover, the true power-law character does not really show until $qR_g \geq 5$. Hence one must beware when data in this regime are limited. An example of structure factor data with an ample power-law regime is given in Figure 23–12. The power-law regime is quite linear in this log–log plot with a slope that yields $D_f = 1.75$.

Polydispersity does not affect the negative fractal dimension slope of the structure factor for $qR_g \geq 5$ except in extreme cases, as yet not encountered in aerosols. Martin and Ackerson (1985) discuss this theoretically.

Measurement of Polydispersity. A well-endowed power-law regime, that is, one that extends out to $qR_g \approx 10$ or more, has another advantage besides easy extraction of an accurate fractal dimension. A measure of the polydispersity can be obtained using the coefficient C_p in Eq. 23–33. In a recent study Sorensen and Wang (1999) proposed the large $qR_{g,z}$ form in Eq. 23–33 to differentiate between single-cluster and polydispersity effects on this regime. The constant C depends on the cut-off function $h(x)$ of the density correlation function, Eq. 23–10. It was

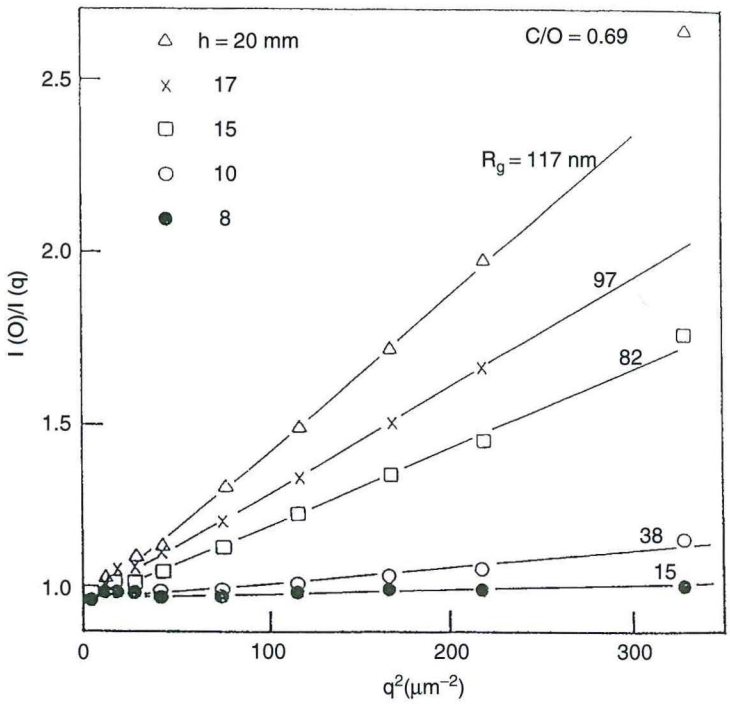

Fig. 23–13. Flame soot aerosol data of Figure 23–11 plotted for a Guinier analysis.

concluded that $C = 1.0 \pm 0.1$ best describes cluster–cluster fractal aggregates. The constant C_p depends solely on the polydispersity of the cluster system and can be used to measure the polydispersity. For further information on this topic, see Sorensen and Wang (1999).

In summary, the measurement of optical structure factor is a very useful method capable of yielding particle R_g, D_f, and the polydispersity. The particle refractive index need not be known. If data beyond $qR_g < 5$ are not available, the D_f measurement can only be considered qualitative. An excellent procedure is to determine R_g with the Guinier analysis using small q data and then D_f with a log–log plot (or fit) using large q data. See Sorensen (2001) for an extensive review of fractal aggregate light scattering.

Shape Factor. Sorensen and co-workers (Cai and Sorensen, 1994; Wang and Sorensen, 1999) have used light scattering to study fractal aggregate diffusivity. This is relevant to the dynamic shape factor because the diffusion coefficient D and the coefficient of the drag force f in $F = fV$ are related by the Einstein relation

$$D = kT/f \tag{23–35}$$

where k is the Boltzmann constant and T is the temperature. Their method used static light scattering to measure the aggregate radius of gyration, R_g, and the fractal dimension D_f and dynamic light scattering to measure the diffusion coefficient. The fractal aggregates were soot in a premixed methane/oxygen flame and TiO_2 aggregates in air at room temperature and pressures from 1/15 to 1 atmosphere. Wang and Sorensen (1999) also reinterpreted aerosol mobility data of Schmidt-Ott (1988) and Rogak et al. (1990) and the colloidal data of Wiltzius (1987) and combined all these with their data to achieve a general picture of the mobility of fractal aggregates at all values of the Knudsen number.

Wang and Sorensen (1999) gave their results in terms of the ratio of the mobility radius, R_{mob}, to the radius of gyration, R_g. To recast their results into the dynamic shape factor, recognize that Eq. 23–1 implies

$$\chi = R_{mob}/R_m \tag{23–36}$$

where R_m is the mass equivalent radius. The mobility radius was defined by the modified Stokes relation

$$F = 6\pi\mu R_{mob}/C(R_{mob}) \tag{23–37}$$

Wang and Sorensen's results (1999) pertain to the common situation of diffusion-limited cluster aggregates, which have a fractal dimension $D_f \approx 1.75$. Under these conditions two regimes of functionality for R_{mob} were found depending on the number of monomers or primary particles (N) per aggregate. When N is small (i.e., ≤60), then

$$R_{mob} = aN^{0.44} \tag{23–38}$$

where a is the monomer radius. This empirical result has the correct $N \to 1$ limit. Because $R_m^3 = a^3N$, it follows from Eqs. 23–36 and 23–37 that

$$\chi = N^{0.11}, \quad N \le 60 \tag{23–39}$$

For large N it was found empirically that

$$R_{mob} = 0.7\ R_g \tag{23–40}$$

R_g is related to N via

$$N = k_o(R_g/a)^{D_f} \tag{23–41}$$

Where $k_o \approx 1.3$. It then follows that

$$\chi = 0.6\ N^{0.24}, \quad N \ge 60 \tag{23–42}$$

Before we discuss these results, we consider two other functional relationships. First, Chan and Dahneke (1981) calculated R_{mob} for straight chains of N individual spheres in the free molecular limit. From this we find

$$\chi = \frac{\sqrt{0.802(N-1)+1}}{N^{1/3}} \tag{23–43}$$

Second, a limiting case, often called the *free draining limit* in polymer science, would be when the drag on an aggregate is the sum of the drags due to the N individual spheres. Then it follows that

$$\chi = N^{2/3} \tag{23–44}$$

All these results, Eqs. 23–39, 23–42, 23–43, and 23–44, are plotted in Figure 23–14. We see that the independent spheres approximation works very poorly. This implies that there is considerable interaction of the flow fields around each monomer. On the other had, the linear chain result agrees fairly well with the fractal aggregate when N is small, especially when $N \le 10$.

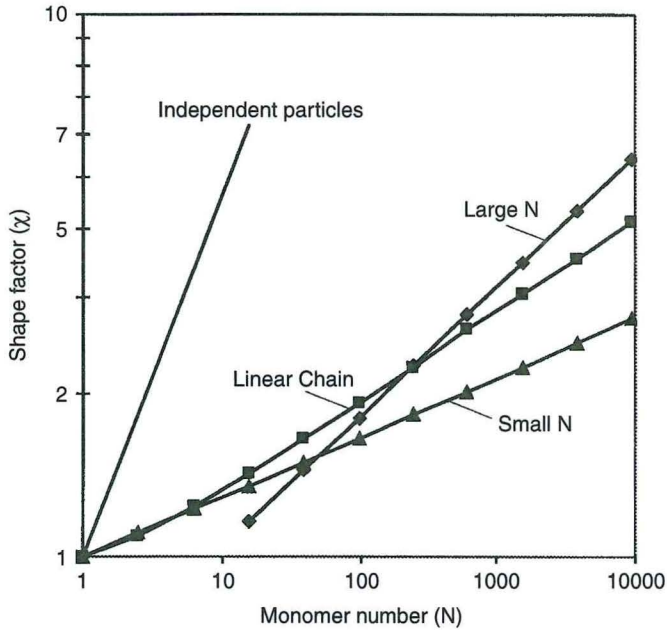

Fig. 23–14. Calculated values of shape factor for several particle agglomerate configurations.

This implies that the geometry of the arrangement of the monomers is not important until N is larger than 10.

Figure 23–14 may be used to determine the dynamic shape factor for fractal aggregates for all values of the Knudsen number. When $Kn \approx 0$, the continuum regime, χ, is given by the greater of the two solid lines, representing Eqs. 23–39 and 23–42, in Figure 23–14. For large Kn, the behavior of χ is less certain. A description for this regime consistent with the conclusions of Wang and Sorensen (1999) is that χ is given by the small N curve whenever $Kn > 5$. For $N > 60$ and $1 < Kn < 5$, we expect χ crosses over smoothly between the small and large N curves as $Kn \rightarrow 0$.

FIBERS

Introduction

The term *fiber* has been applied to a wide variety of particles having an elongated shape (i.e., one particle dimension significantly greater than the other two). Because of this elongation, fibers can have aerodynamic and other properties quite different from more compact particles. Certain fibers have several unique properties that make them not only useful from a commercial standpoint but also important from a health standpoint. Asbestos, for instance, includes six commercial fibrous minerals that have high tensile strength, chemical resistance, and excellent thermal and acoustic insulation characteristics. These properties have made asbestos useful in a variety of products, including friction materials, high-temperature insulating materials, acoustic insulation, fire-proof cloth and rope, and floor tiles. While the bulk materials in these products may consist primarily of macroscopically sized fibers, many of them can release long, thin fibers into the air.

A variety of materials can be considered fibers from an aerosol behavior standpoint. Besides asbestos, other mineral fibers exist in nature. Several materials, including glass and mineral slags, have been melted and spun into fibers. Ceramic materials have similarly been spun into fibers, as well as grown by chemical and vapor crystallization. Carbon and graphite fibers are produced commercially for high-strength products. Organic fibers, such as cotton, wood, and other cellulosic materials, are widely present in the environment, from both commercially produced materials and natural sources. Carbon "nanotubes" are a tubular form of carbon "buckyballs" (C_{60}), a molecular structure of pure carbon with very high strength and high conductivity (Ren et al., 1998). These nanotubes are being commercially developed for a variety of applications. Besides cylindrical particles that have relatively high strength, chains of particles also may behave as fibers and can serve as models for some aerodynamic properties of fibers. Some organic materials can be crystallized into well-defined fibrous shapes and can be used to test theories of fiber aerodynamic behavior.

Asbestos fiber aerosols have been closely associated with several diseases, such as asbestosis (a fibrosis of the lung), mesothelioma (cancer of the lining around the lung), and lung cancer (National Institute for Occupational Safety and Health, 1976). Thus, the fibers that can enter the respiratory system are of greatest concern. The seriousness of the diseases has driven measurement technology to provide maximum sensitivity and accuracy for measuring asbestos aerosols. Other airborne fibers may have one or more of the same physical and chemical properties as asbestos. In some cases, human exposures and/or animal studies suggest the disease potential of these fibers. Thus, there is concern regarding the health effects of fibers other than asbestos. While the commercial properties of mineral fibers have created a store of knowledge about physical and geologic properties, it is the health concerns that have largely driven the technology for detecting and quantifying airborne concentrations of fibers. Thus, much of the fiber aerosol research and measurement capability relates to the ability of microscopically sized fibers to enter, deposit, and remain in the human respiratory system.

The dimensions of fibers in aerosols can cover a wide range. Asbestos consists of material composed of individual fibrils as small as 0.025 μm (Langer et al., 1974). Airborne fibers can be single fibrils or various-sized bundles with a range of diameters, while lengths can be less than 0.5 μm to several hundred micrometers. The dimension distributions depend on the fiber type as well as on how the fibers were comminuted from the bulk material. The magnitude of disparity between length and diameter often makes it difficult to make accurate size distribution measurements. Several protocols, using various types of microscopes, have been developed to deal with fiber distribution measurement. Other types of instruments, primarily using light-scattering properties, have been developed to characterize fibers. However, these instruments usually provide only an approximate indication of fiber dimensions.

Note that the following discussion, except where otherwise indicated, deals largely with measurement of aerosolized fibers, generally visible only with a microscope, and not with the macroscopic or bulk properties of the fibrous material. Because asbestos has been the most intensely studied type of fiber, many comments will relate to this material. Many issues regarding asbestos mineralogy, health effects, and measurement techniques are discussed in a review by Walton (1982); further reviews in Environmental Health Perspectives are introduced by Langer (1974) and Dement (1990). Additional topics are presented in books by Selikoff and Hammond (1979), Rajhans and Sullivan (1981), Michaels and Chissick (1979), Chissick and Derricott (1983), and Holt (1987). Similar reviews have been carried out for manmade fibers (National Institute for Occupational Safety and Health, 1976, 1977; IARC, 1988).

Fiber Shape

The behavior of fibers suspended in a gas is a function of the fiber dimensions. Assuming either a cylindrical or prolate spheroidal shape, these dimensions can be defined by two para-

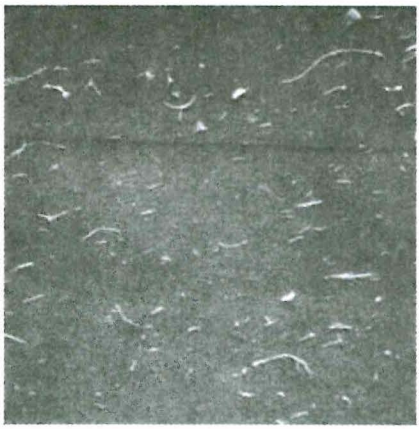

Fig. 23–15. Scanning electron micrograph (×1500) of an aqueous sample of magnetically aligned UICC Canadian chrysotile collected on a 0.1 μm pore size filter. (From Timbrell, 1973.)

meters, length and diameter. A third parameter β is often invoked to indicate the fibrosity or aspect ratio (i.e., the ratio of the length to the diameter). However, real fibers frequently do not meet the either the ideal cylindrical or the prolate spheroid shape assumption. Glass or mineral fibers are often nearly cylindrical, but even these fibers frequently display curvature along their length as well as bulbous or jagged ends. Asbestos fibers are formed from a unique crystal habitat in which the bulk mineral has slip planes in two directions, but only rarely in the third. This results in a propensity to produce particles that can split longitudinally to produce thinner and thinner fibers, ultimately resulting in fibrils about 0.02 to 0.05 μm diameter. Thus, while some asbestos fibers exhibit a nearly ideal cylindrical shape, others may have various combinations and degrees of splayed ends, curvature, splitting, noncircular circumference, and so forth. For instance, the magnetically aligned chrysotile fibers in Figure 23–15 show many of these characteristics. Despite these possible variations in shape, fibers are still most often characterized simply by length and diameter.

Distributions of natural fibers are rarely monodisperse in diameter and even more rarely in length. This has made it difficult to provide adequate calibration for instruments that attempt to measure fibers as well as to perform measurements of fiber toxicity as a function of fiber dimension. Distributions of fibers can often be described by a two-dimensional (length L and diameter W) lognormal distribution (Schneider et al., 1983; Cheng, 1986), that is, $\ln L$ and $\ln W$ are each distributed normally. The probability density function is given by

$$f(L,W) = \frac{1}{2\pi\sigma_w\sigma_L\sqrt{1-\tau^2}LW}\exp\left(-\frac{A^2+B^2-2\tau AB}{2(1-\tau^2)}\right) \tag{23–45}$$

where $A = (\ln W - \mu_W)/\sigma_W$ and $B = (\ln L - \mu_L)/\sigma_L$.

μ_i and σ_i^2 are the mean and variance of the natural logarithm of L and W, respectively, and τ is the correlation between $\ln L$ and $\ln W$, τ ranges from −1 to 1. The five parameters μ_L, μ_W, σ_L, σ_W, and τ are needed to define completely a two-dimensional size distribution. The two-dimensional lognormal size distribution has the properties that the marginal and the conditional distributions are lognormal (Holst and Schneider, 1985). The former property indicates that the length and diameter distributions are each separately lognormal. The latter indicates that functions of length and diameter of the form kW^pL^q, where k, p, and q are constants, are also lognormal. Such functions include aspect ratio, surface area, volume, and aero-

TABLE 23–1. Examples of Measured Fiber Size Distributions

Material	Diameter (μm)	σ_g	Length (μm)	σ_g	MMAD (μm)	σ_g	Measurement Technique
Chromoglycic acid[1]	0.205	1.58	2.09	1.83			SEM
					0.65	1.88	Cascade Impactor
Sugar cane silicate[2]	0.3–1.5*		3.5–65*				TEM
Caffeine[3]	1.13	1.08	5.55	1.12			SEM
					2.1	1.1	Sedimentation
Ceramic fibers[4]							
sample a	0.5		10.1				TEM
sample b	0.66		8.3				TEM
sample c	0.98		22.8				TEM
Chrysotile[5]							
Preform ring	0.13	2.15	1.6	2.7			TEM
Yarn dressing	0.08	1.92	1.0	2.4			TEM
Cure press	0.13	1.94	1.5	2.2			TEM
Crocidolite[6]							
Mine/Mill**	0.08–0.10	1.86–2.08	0.98–1.25	2.30–2.55			TEM
Manufacturing	0.04	1.58	0.54	2.32			TEM
Fibrous glass[7]							
Code 100	0.12	1.8†	2.7	2.2†			TEM
Code 110	1.8	1.7†	26	2.0†			TEM
Iron Oxide Chains[8]							
	0.059	1.1	1††	2.0			TEM
					0.32	1.11	Centrifuge

*These values represent the range of particle sizes rather than the median diameters.
**These values represent the range of several measurements that produced similar results.
†Estimated from data in reference.
††Estimated from mean chain length of 22 primary particles.
[1]Chan and Gonda (1989).
[2]Boeniger et al. (1988).
[3]Vaughan (1990).
[4]Rood (1988).
[5]Rood and •• (1989); Pinkerton et al. (1983).
[6]Hwang and Gibbs (1981).
[7]Timbrell (1974).
[8]Kaspar and Shaw (1983).

dynamic diameter. Deviations from lognormality can sometimes be attributed to artifacts in sampling or analysis or to multiple aerosol generation sources.

Many fiber distributions reported in the literature include the length and diameter means and variances, but unfortunately do not include τ. However, if the original data are reported in a table as a function of both length and diameter, the correlation term can be estimated (Cheng, 1986). Most fiber distributions have positive τ, suggesting that diameter often increases with length.

There have been measurements of a variety of fibrous aerosols. Table 23–1 lists the results of some examples. Some of these materials have been generated for toxicity studies, some have been measured in environmental studies, while others have been generated as calibration materials.

Fiber Behavior

Translational Motion. As with other aerosol particles, fiber dimensions can cover a relatively wide range: The smaller fibers are affected primarily by diffusional forces, while the larger ones are primarily affected by flow shear and inertial and gravitational forces. Fiber

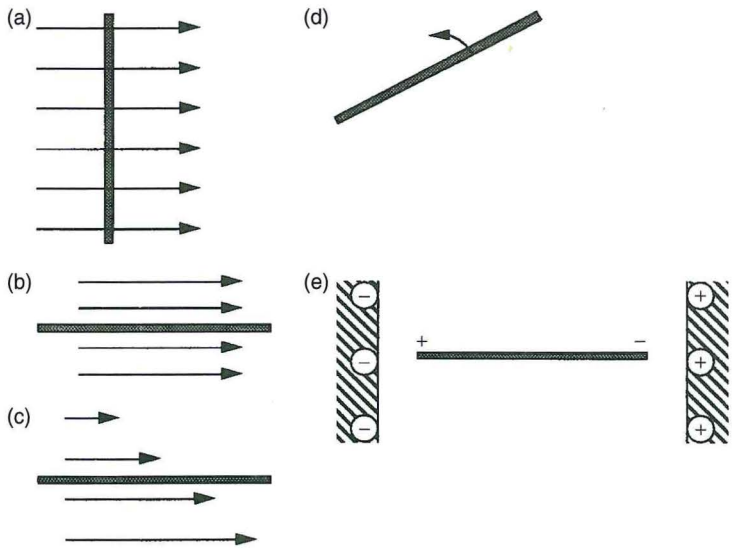

Fig. 23–16. Fiber alignment in various force fields. **a**, Fiber aligned perpendicular to relative gas motion. This is the preferred orientation during gravitational settling and acceleration at $0.01 < \mathrm{Re} < 100$ in the absence of other forces. **b**, Fiber parallel to relative gas motion. Fiber motion is often treated as a combination of cases a and b. **c**, Fiber is readily oriented parallel to, or at some small angle to, the direction of shear flow in the suspending gas medium. **d**, Small fibers governed by diffusional forces may exhibit completely random orientation. **e**, Conductive fibers are aligned parallel to an electric field. Many fibers are also aligned in a magnetic field, usually parallel to the field lines, though they may be aligned perpendicular to the field or, for some materials, at some intermediate angle.

behavior has been observed and theoretically calculated for several fibrous shapes, including prolate ellipsoids, cylinders, and chains of spheres. The motions of these various shapes generally differ only slightly.

Fiber behavior differs depending on whether the major axis is oriented parallel or perpendicular to the direction of the motion relative to the surrounding gas (Fig. 23–16a,b). The drag on a fiber is greatest when it is oriented perpendicular to the flow of the surrounding gas. Fiber behavior is often described in terms of a combination of the two orientations. While the difference in drag between the two orientations is typically about 15% to 30%, it can be difficult to determine the contribution of each orientation in experimental systems. At low Reynolds number (Re_p), fiber orientation will be stable (discounting Brownian rotation) and not change due to translational motion, for example, during gravitational settling (Gallily, 1971). In addition, fibers settling in still air will not settle exactly in the direction of the gravitational force, but will drift somewhat due to orientation (Weiss et al., 1978). Larger fibers, with Re_p greater than about 0.01 will settle with their major axis oriented perpendicular to the direction of motion (Fig. 23–16a). With increasing Re_p ($Re_p > 100$), longer fibers ($\beta > 20$) are still stable in the perpendicular orientation, but there is an increasing trend toward instability (Clift et al., 1978:154).

The aerodynamic diameter d_a of a prolate spheroid has been calculated

$$d_a = d_f \sqrt{\frac{\rho_f \beta}{\rho_0 \chi}} \tag{23–46}$$

by using the numerical shape factor χ of a prolate ellipsoid of revolution (Fuchs, 1964) d_f is the physical fiber diameter, ρ_f is the fiber density, and ρ_0 is standard density. A

cylinder with the same diameter and length as a prolate ellipsoid has 3/2 greater volume and mass. Therefore, for cylinders with the same axial dimensions, the right-hand side of Eq. 23–2 must be multiplied by $(3/2)^{1/3}$ or $(3/2)^{1/2}$ to obtain the equivalent volume diameter or equivalent weight diameter, respectively (Griffiths and Vaughan, 1986). For motion parallel and perpendicular to the fiber major axis, the respective shape factors $\chi_{\parallel}^{\lambda}$ and $\chi_{\perp}^{\lambda}$ are

$$\chi_{\parallel} = \frac{4(\beta^2-1)}{3} \Bigg/ \left\{ \frac{2\beta^2-1}{\sqrt{\beta^2-1}} \ln\left(\beta+\sqrt{\beta^2-1}\right) - \beta \right\} \tag{23–47}$$

$$\chi_{\perp} = \frac{8(\beta^2-1)}{3} \Bigg/ \left\{ \frac{2\beta^2-3}{\sqrt{\beta^2-1}} \ln\left(\beta+\sqrt{\beta^2-1}\right) + \beta \right\} \tag{23–48}$$

(see Fig. 23–16a,b). Note that a dynamic shape factor χ_d is also defined that is related to the numerical shape factor for prolate spheroids by $\chi = \chi_d \beta^{-1/3}$ (Stöber, 1972; Kasper, 1982). The dynamic shape factor is applied when the equivalent volume diameter of the particle is used rather than the physical diameter.

An alternate approach for directly calculating the aerodynamic diameter of cylinders (Cox, 1970) gives similar results:

$$d_{a,\parallel} = d_f \sqrt{\frac{9\rho_f}{4\rho_0}[\ln(2\beta) - 0.807]} \tag{23–49}$$

and

$$d_{a,\perp} = d_f \sqrt{\frac{9\rho_f}{8\rho_0}[\ln(2\beta) + 0.193]} \tag{23–50}$$

Others have also provided formulas for prolate ellipsoids and cylinders (Gonda and Khalik, 1985).

If fibers are not preferentially oriented by a drag force or other alignment force, the orientation may be completely random. Then, a single average shape factor $\bar{\chi}$ that is a function of the two noted above may be used

$$\bar{\chi} = \beta^{1/3}\left(\frac{1}{3}\chi_{\parallel} + \frac{2}{3}\chi_{\perp}\right) \tag{23–51}$$

In the presence of air gradients, the fiber will experience a torque until the fiber is oriented parallel to the direction of shear force (Fig. 23–16c). Thus, a fiber settling in a horizontal laminar flow will tend to be oriented horizontally (parallel to the shear). However, the fiber will experience a periodic instability and perform a "flip." This instability is a function of fiber dimensions as well as the flow gradients. Under such conditions, the aerodynamic diameter is not strictly an inherent property of the particle and depends on the experimental conditions of measurement (Gallily and Eisner, 1979).

Inertial separation is commonly used for particle separation and sizing (e.g., in impactors and cyclones). In such systems where flow conditions are rapidly changing, the fiber mechanics are governed by initial orientation and flow relaxation time besides the usual parameters observed for spherical particles (Gallily et al., 1986). For instance, fibers with large rotational inertia (especially long fibers) may not orient completely or may over-rotate in passing through a nozzle. Fiber behavior under such a situation may be only approximately defined by Stokes number or other nondimensionalized parameters.

Experimental measurement of fiber deposition has been carried out in horizontal elutriators (Gallily and Eisner, 1979; Griffiths and Vaughan, 1986; Iles, 1990), centrifuges (Stöber et al., 1970; Martonen and Johnson, 1990; Asgharian and Godo, 1999), impactors (Burke and

Esmen, 1978; Prodi et al., 1982; Asgharian et al., 1997), and cyclones (Fairchild et al., 1976; Iles, 1990) for a variety of fiber types.

The extended shape also means that interception during translational motion plays a larger role in fiber deposition than for compact particles. However, the alignment of fibers by shear flow often reduces the effect of length on interception.

Rotational Motion. The rotational mobility B_r of a high aspect ratio ellipsoid can be approximated by (Lilienfeld, 1985)

$$B_r = \frac{3[2\ln(2\beta - 1)]}{2\pi\eta L^3} \tag{23–52}$$

where η is the viscosity of the gas. Note that the rotational mobility is a strong inverse function of fiber length. Similarly the rotational diffusion coefficient D_r for fibers is also a strong function of fiber length

$$D_r = \frac{3kT}{\pi\eta\beta L^3}(\ln 2\beta - \delta) \tag{23–53}$$

where k is the Boltzmann constant, T is temperature, and δ is 1.4 for aspect ratios β larger than 10. Rotational mobility can be estimated by measuring the rate of relaxation after removal of an electrostatic alignment force (Cheng et al., 1991).

Behavior in the Transition Regime. Under molecular bombardment, fibers can exhibit both rotational diffusion and translational diffusion. Such fibers are likely to be randomly oriented (Fig. 23–16d). As for fibers in the Stokes regime, it is often convenient to separate the translational motion of fibers into motion in which the major axis is parallel to the direction of motion and another in which the major axis is perpendicular to the translational motion. Diffusion of fibers is described by the diffusion coefficient D_f (m^2/s)

$$D_f = BkT = \frac{kT}{f} = \frac{kTC_f}{f^0} \tag{23–54}$$

where B is the fiber mobility (dyne-cm/s), f^0 is the drag per unit velocity of the fiber in the continuum regime, and f is the drag per unit velocity of the fiber corrected for slip by the fiber slip correction factor C_f. A theory for the slip correction factors for nonspherical particles is described by Dahneke (1973a–c, 1982).

Fiber diffusional behavior is usually treated as a modification of spherical particle diffusion using particle shape factors (Asgharian and Yu, 1988). This approach has agreed well with experimental diffusion coefficient measurement of fibers with mean diameters between 0.24 and 0.38 μm (Gentry et al., 1983). Diffusional coefficients of much smaller fibers have also been measured (Gentry et al., 1988) that show higher diffusion coefficients than expected.

As with the stagnant flow conditions for fibers in the continuum regime, fibers are expected to be randomly oriented unless affected by shear flow or other forces. Again, the longer the fiber, the more likely it is to be oriented by such forces.

Several studies have estimated effects of various deposition mechanisms (diffusion, impaction, interception) to determine overall particle deposition in filters (Fu et al., 1990) and lung airways (Asgharian and Yu, 1989; Balásházy et al., 1990; Asgharian et al., 1997).

Charging. Theories for unipolar diffusion charging (Laframboise and Chang, 1977) and bipolar diffusion charging (Wen et al., 1984) of fibers have been developed. Unipolar charg-

ing of fibers causes the charge of long, thin fibers to increase dramatically, though the electrical mobility of such fibers changes more slowly with aspect ratio (Yu et al., 1987). Such a variation of mobility with fiber aspect ratio may allow separation of fibers of different lengths.

Electric Field Effects. A fiber may be aligned in an electric field by an induced dipole in the fiber. This requires that charges in the fiber be separated so that the polarity is opposite to that of the surrounding electric field as shown in Figure 23–16e. The charge separation from conduction is usually greater than from polarization of the material. For charge separation to occur, the fiber must be sufficiently conductive so that the charges can migrate the length of the fiber in a reasonable time. Aerosol particles, even those consisting of a normally nonconducting material, can often be considered conductive because of their low capacitance and small dimensions (Fuchs, 1964; Lilienfeld, 1985). Surface impurities can also contribute to a particle's conductivity. In addition, water adsorbed on the fiber surface (e.g., glass fibers at approx. 50% relative humidity) can increase the conductivity and allow fiber alignment in an electric field. Thus, an electric field of sufficient strength (1×10^5 to 5×10^5 V/m) can overcome diffusional randomization and flow shear forces to align most types of fibers, including relatively nonconductive ones. For instance, electrostatically aligned zinc oxide fibers were used to modulate microwave radiation (Tolles et al., 1974).

When fibers and compact particles of the same aerodynamic diameter are charged under the same conditions, the fibers may have higher mobility than compact particles. Field studies of work environments suggested that fibers carried a charge proportional to fiber length (Johnston et al., 1985). Other studies indicated that unipolar, charged particles can be separated according to aspect ratio (Griffiths et al., 1985; Yu et al., 1987).

Electrostatic enhancement of fiber deposition in lungs (conductive tubing) has been observed (Jones et al., 1983). Calculations support such enhancement of sedimenting charged fibers (Chen and Yu, 1990).

Dielectrophoresis. Dielectrophoresis was investigated for separating aluminum wires of different lengths in liquid suspension (Lipowicz and Yeh, 1989). The velocity of conductive fibers with an aspect ratio >3 in a gradient electric field was given by Eq. 18–50, indicating that the fiber velocity was proportional to the electric field squared and the fiber length squared. Baron et al. (1994) demonstrated that fiber length classification could be achieved for fibers as short as 4 μm in a 0.76 m long classifier. This technique has been used for production of small quantities of classified fibers for in vitro cell assay studies and for fiber size measurement (Baron et al., 1998; Ye et al., 1999). For further discussion of this technique, see Chapter 18.

Magnetic Field Effects. If a suspension of fibers in a liquid or gas is subjected to a magnetic field, fibers with sufficient magnetic susceptibility will align at some angle to the field. Usually this angle is either 0° or 90°; some amphibole asbestos samples have fibers aligned at both angles. Timbrell (1975) developed a technique for preparing permanently aligned samples by allowing a suspension of fibers in 0.5% celloidin/amyl acetate to dry in a 5000 to 10,000 gauss magnetic field. Several fiber types have been aligned by Timbrell (1972, 1973), including carbon fibers and the various types of asbestos. Fibers of glass, silicon carbide, silicon nitride, and tungsten-cored boron did not align in similar fields.

Figures 23–17, 23–18, and 23–19 contain images of fibers magnetically aligned on a slide surface with light-scattering patterns from magnetically aligned liquid suspensions of the same types of fibers. The direction of the magnetic field is shown in the figures. The scattering pattern has the main laser beam in the center, with the plane of scattering radiating in opposite directions. In Figure 23–17, monodisperse diameter carbon fibers all are aligned parallel to the field so that a well-defined scattering pattern perpendicular to the field is

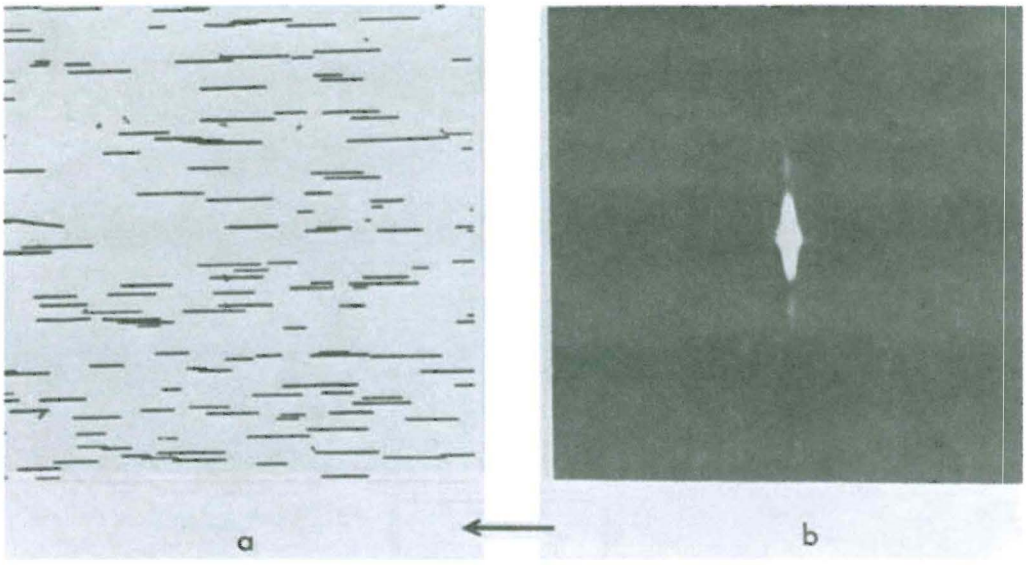

Fig. 23–17. **a**, Phase contrast microscope (PCM) image of magnetically aligned carbon fibers suspended in celloidin on a glass slide. **b**, Light-scattering pattern from the same fibers in aqueous suspension. The direction of the magnetic field is indicated by the arrow. Note the monodisperse diameter of the fibers, reflected in the sharply defined scattering pattern. (From Timbrell, 1973.)

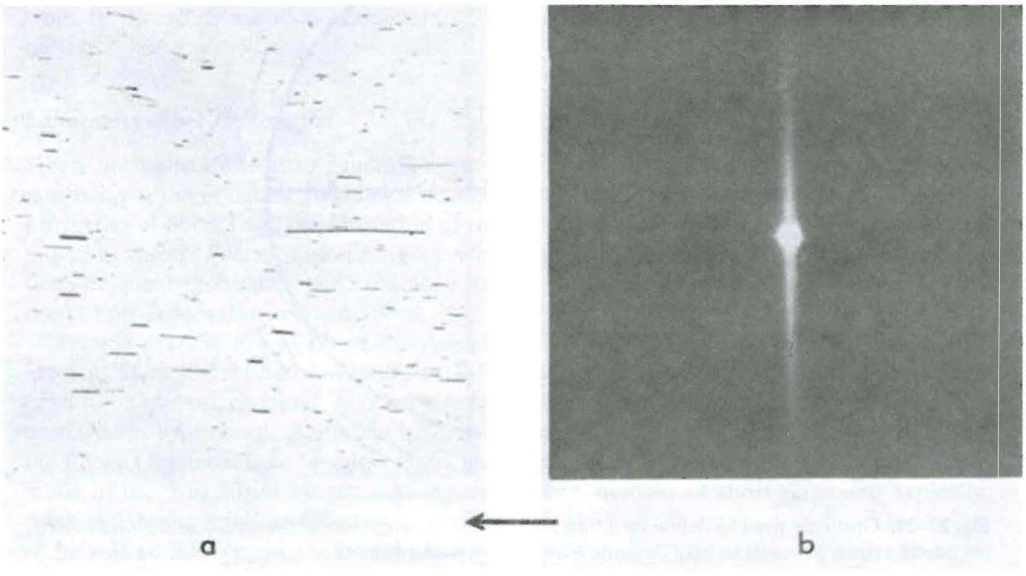

Fig. 23–18. **a**, PCM image of magnetically aligned UICC crocidolite fibers suspended in celloidin on a glass slide. **b**, Light-scattering pattern from the same fibers in aqueous suspension. The direction of the magnetic field is indicated by the arrow. (From Timbrell, 1973.)

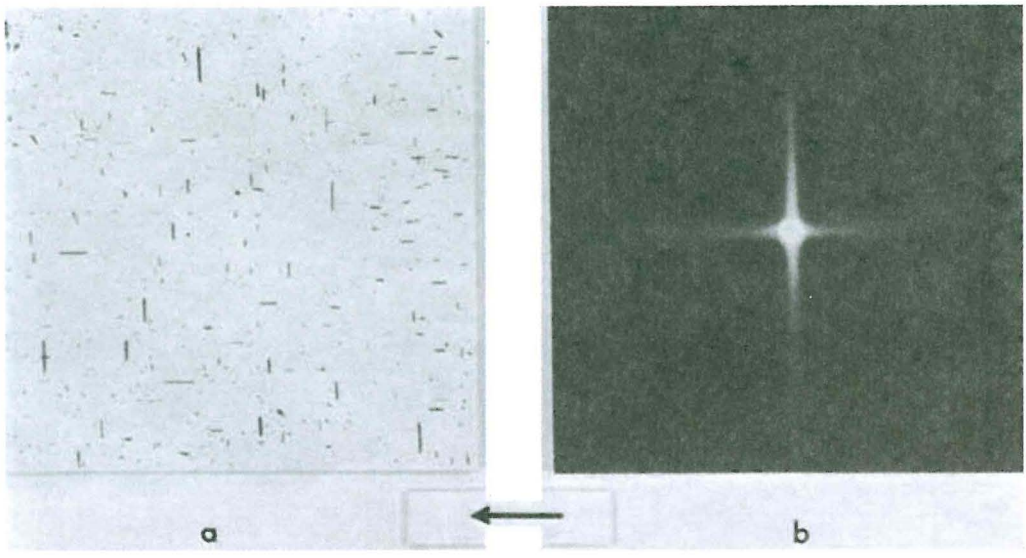

Fig. 23–19. **a**, PCM image of magnetically aligned UICC amosite fibers suspended in celloidin on a glass slide. **b**, Light-scattering pattern from the same fibers in aqueous suspension. The direction of the magnetic field is indicated by the arrow. (From Timbrell, 1973.)

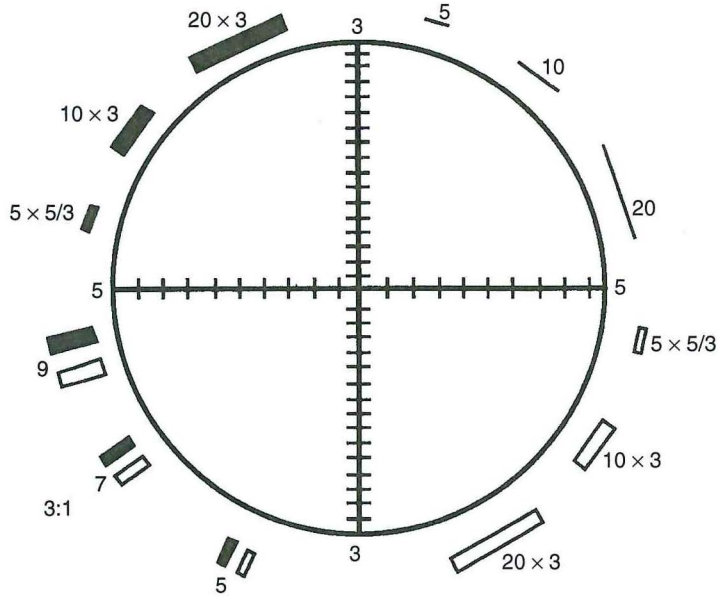

Fig. 23–20. Graticule used to define counting field in a phase contrast microscope. The defined objects outside the circle are used to help determine aspect ratios and sizes of fibers that should be counted.

produced. The crocidolite fibers in Figure 23–18 are aligned the same way, but are not monodisperse. In other cases, the fibers are aligned perpendicular or both perpendicular and parallel to the magnetic field (e.g., Fig. 23–20), the latter resulting in two planes of scattering. A synthetic fluoroamphibole was observed to align at ±65° to the magnetic field direction.

The degree and direction of alignment have not been adequately explained; however, they appear to be more a function of the mineralogical source of the material than of the primary crystal structure. Thus, Ugandan tremolite was observed to align perpendicular to the magnetic field, while Zululand tremolite aligned parallel to the field (Timbrell, 1973).

Light Scattering. With a flashlight beam shining on a glass rod such that the light beam was perpendicular to the rod axis, one would expect the refracted and scattered light to be dispersed into a plane perpendicular to the rod's axis. Light scattered and refracted from microscopic fibers produces a similarly unique pattern. Such scattering patterns from magnetically aligned fibers in an aqueous suspension are given in Figures 23–17, 23–18, and 23–19. If the fiber is not perpendicular to the light beam, the light-scattering pattern is not as conveniently constrained to a plane, becoming a cone of light. The details of light scattering from infinitely long cylinders, ellipsoids, and several other regular elongated shapes can be described with Mie theory (Van de Hulst, 1957; Kerker, 1969). As with scattering from spherical and compact particles, the scattering from fibers with diameters larger than the light wavelength is concentrated in the forward direction. The scattering from smaller diameter fibers is less in magnitude, but more uniform in all directions around the fiber axis. In addition, the scattered light tends to be polarized in the direction parallel to the fiber axis.

The unique, planar scattering pattern for right-angle illumination has been the basis of several useful fiber detection techniques. As noted above, the fiber must be held perpendicular to the light beam axis to obtain the characteristic fiber pattern. A fiber collected on a surface such as a glass slide will generally be parallel to the slide surface, thus allowing a beam perpendicular to the slide surface to produce the narrow, planar scattering pattern from a single fiber. To obtain a characteristic scattering pattern from a group of fibers, they must be aligned using some force, such as magnetic, electric, or shear flow.

Figures 23–17, 23–18, and 23–19 show the scattering patterns for several types of fibers. Note the well-defined scattering pattern for monodisperse carbon fibers (Fig. 23–17), while the broad distribution of diameters for the other fiber types produces a more diffuse pattern.

Laboratory Fiber Generation

Fibers are more difficult to generate than compact particles because of their tendency to intertwine when in contact with each other. This tendency is the basis for some commercial properties of fibers (e.g., the formation of rope and felt). Various types of fibers can be generated in various concentration ranges for instrument calibration, analytical method validation and quality assurance, and toxicology studies. Various generation mechanisms have been used to produce well-dispersed fibers.

Sample preparation of fibers for generation is an important step in producing useful aerosols. Some fibers may be available in sufficiently comminuted form for generation. Others need to be ground, chopped, or otherwise reduced in size. Blenders and grinders have been used. Air or water suspensions can be elutriated to reduce primarily the diameter range of the fibers. One technique for glass fibers used compression to produce fiber lengths with a mode in the 5 to 20 μm range, reducing the relative number of short fragments typically produced during grinding (Hanton et al., 1998).

Nebulization of liquid suspensions has been used for generating relatively short fibers at low concentrations. Fibers larger than the nebulized droplet diameter may not be generated efficiently, and, if the concentration is too high, more than one fiber may be present in a droplet, resulting in fiber agglomerates.

Several researchers have used high-speed chopping of a packed fiber plug. Timbrell et al. (1968b) developed a version of this approach using a household coffee grinder. A specially ground reference material, Union Internationale Contre le Cancer (UICC) asbestos

(Timbrell et al., 1968a), was packed uniformly in a syringe body and pushed slowly into the rotating blades of the grinder. The consumption rate of asbestos was 0.6 to 1.0 g/h, though not all this was generated as an aerosol. The dispersion appeared to be largely single fibers with relatively few clumps or flocculates, though no size distribution was reported. A generator with similar operating principle and dimensions was constructed using more durable materials, including tungsten carbide blades and a stainless steel body (Fairchild et al., 1976). This device was used for both chrysotile and fibrous glass. Although there were relatively few clumps of chrysotile by number, the mass in these clumps accounted for the largest fraction of the mass distribution. Airborne concentrations of 6 to 8 mg/m^3 were achieved, though the feed rate could be lowered to one fourth or increased to 10 times the value used for this measurement. Fibrous glass aerosols were more successfully generated with this device (Fairchild et al., 1978).

Fluidized bed generators have also been used for creating fibrous aerosols. Fluidized beds usually consist of two phases: a powder phase, containing one or more components, and an air phase passing through the powder. The powder is made to act like a boiling fluid by passing a sufficietly high air flow through it or by applying vibrational or acoustic energy. The powder may consist solely of the dust to be generated, or it may consist of the dust plus particles that are too large to be carried away by the airflow. These larger particles separate the dust particles from each other and tend to break apart agglomerates.

A two-component fluidized bed was used for inhalation exposure experiments with fibrous glass (Carpenter et al., 1981) and crocidolite (Griffis et al., 1983). The bed consisted of a stainless steel powder mixed with the fibers as a slurry and then dried. Air passing through the bed fluidized the bed and released the fibers, initially at a high rate and then decreasing exponentially. A similar air-fluidized bed with bronze powder as the fluidizing powder was used for generating multiple filter samples of chrysotile for a quality assurance program (Baron and Deye, 1987).

Charge must be reduced on generated aerosols to produce uniform air concentrations and consistent measurements. This can be accomplished by charge neutralizers (see Chapter 19) or by modifying the generation conditions. It was found that fluidized beds produced highly charged fibers when operated with dry air. The charge level dropped about 10-fold when the relative humidity of the air was increased to about 15% (Baron and Deye, 1990).

A two-component fluidized bed generator with a screw feed system to continually refresh the bed with premixed powder was found to produce a constant output concentration (Tanaka and Akiyama, 1984). This generator, using glass beads as the large particle fluidizing component, was found to produce a constant 6 mg/m^3 fibrous glass (from a glass fiber filter) for 1 week (Tanaka and Akiyama, 1987). A similar system using stainless steel beads and asbestos fibers was developed by Sussman et al. (1985).

An acoustically fluidized bed was developed to generate cellulose, ceramic, and glass fibers (Weyel et al., 1984; Frazer et al., 1986; Craig et al., 1991; Blake et al., 1997). This design allowed introduction of bulk fibrous powder into the generator with relatively little processing and produced reasonably constant output concentrations over long periods of time.

A one-component fluidized bed developed by Spurny (1980; Spurny et al., 1975) used vibrational energy to assist bed fluidization. The output of the bed for several types of asbestos was constant with time, and the fiber size was somewhat controlled by the vibration frequency and amplitude. A fluidized bed generator of this type using mechanical vibration is commercially available (***PAL***).

Chains of iron oxide particles have been generated using a laminar carbon monoxide flame (Kasper et al., 1980). This generation system created a high concentration of relatively monodisperse ($\sigma_g \approx 1.4$), nearly spherical particles that, under appropriate conditions, agglomerated into chains with little branching, perhaps due to alignment of magnetic dipoles in the agglomerating particles. Similar chains have been observed in other flame and arc systems.

An example particle chain size distribution is noted in Table 23–1. These chains can be used for investigating fiber diffusion, alignment, and aerodynamic size, especially in the transition regime (Kasper, 1983).

Fiber Health Effects

While asbestos fibers have many useful commercial properties, there has been much concern regarding their ability to cause disease. There are three primary diseases that have been attributed to asbestos fiber exposure: asbestosis (a fibrosis or scarring of the lung tissue), mesothelioma (a cancer of the pleura or peritoneum), and lung cancer. Other cancers (e.g., of the gastrointestinal tract) also have been attributed to asbestos exposure. Despite an abundance of research into disease mechanisms of asbestos fibers, the etiologies of these diseases are still not well understood. Fiber shape appears to play a major role, although other properties, such as fiber chemistry and solubility in body fluids, clearly are also important.

Fiber diameter must play a role in disease because the aerodynamic properties resulting in respiratory system deposition are strongly dependent on diameter (Timbrell, 1982). In general, mineral fibers must be smaller than about 2 to 3 μm diameter to reach the thoracic region and thinner still to reach the air exchange regions of the respiratory system (Stöber et al., 1970). It has been hypothesized that short fibers have much less disease potential because macrophages in the lung can engulf these particles and remove them from the lung with relative ease. Longer fibers cannot be completely engulfed by these cells and therefore tend to remain in the lung much longer (Holt, 1987). Timbrell (1982) found that clearance occurred for fibers up to 17 μm long, approximately equal to the human macrophage diameter. Use of the dielectrophoretic fiber length classifier to produce small quantities of length-classified fibers in combination with macrophage assays has confirmed that macrophages are damaged and killed by fibers slightly longer than the macrophage diameter. During macrophage death, an "oxidative burst" occurs, and the macrophage produces a series of factors that are linked to lung inflammation and ultimately fibrosis (Blake et al., 1997; Ye et al., 1999).

Besides shape, the chemical properties of fibers also appear to play a role. Some fibers, especially glass, have been found to dissolve in lung tissue over an extended period, reducing their potential for disease (Johnson et al., 1984; Law et al., 1990). Chrysotile fibers longer than 5 μm were found to increase in number in lung tissue, apparently due to longitudinal splitting of the fibers (Bellmann et al., 1986). In vitro studies have suggested that surface properties of fibers also can affect cell toxicity (Light and Wei, 1977).

Extrapolation of these properties indicates that long (especially those >17 μm long), thin (<3 μm diameter) insoluble fibers may have significant disease potential; for example, several researchers have postulated more specific size ranges as causing the various diseases (Pott, 1978; Lippmann, 1988; Timbrell, 1989).

Fiber Regulations

The potentially severe health effects of asbestos fiber exposure have prompted several regulatory and health research organizations to publish regulations and guidelines for controlling airborne concentrations of asbestos fibers. Because the health-based data indicate that disease at current exposure concentrations is primarily related to fiber number, most regulatory air concentration measurements are based on asbestos fiber number concentration rather than on mass concentration. In the United States, for example, the Occupational Safety and Health Administration (OSHA) provides regulations for exposure to hazardous agents in industrial and other workplace settings. The OSHA regulations require that workers are

not to be exposed to more than 1×10^5 fibers/m^3 [0.1 asbestos fibers/cc] averaged over an 8 h period or more than 1×10^6 fibers/m^3 [1.0 fiber/cc] over 30 min as measured using the filter collection/phase contrast microscope (PCM) method (Occupational Safety and Health Administration, 1986). The Mine Safety and Health Administration (MSHA) regulates exposures in mines and mills and limits miner exposure to 2×10^6 fibers/m^3 [2.0 fibers/cc] for an 8 h average and 1×10^7 fibers/m^3 [10 fibers/cc] for a 15 min period (Mine Safety and Health Administration, 1988).

The Environmental Protection Agency (EPA) regulates environmental levels of pollutants. Apart from prohibiting visible emissions, the EPA has not implemented limits for environmental concentrations of asbestos. However, to protect children from being exposed to asbestos in schools, the EPA has mandated procedures for removing and measuring asbestos in schools (Environmental Protection Agency, 1987). The EPA has defined asbestos-containing material (ACM) as material containing more than 1% asbestos, to be measured using polarized light microscopy. After removal of ACM in schools, the EPA requires that the airborne asbestos concentration in the cleaned area be no greater than that outside the area. Measurement is conducted using five air samples inside the area and five outside for the comparison. Analysis by transmission electron microscope (TEM) is required for monitoring the completion of all asbestos removal operations, except that the PCM can be used when removing small amounts of asbestos. Guidance documents describing methods for controlling asbestos in buildings (Environmental Protection Agency, 1985, 1990) and for measurement of asbestos after removal (Environmental Protection Agency, 1985) have been provided.

Because ceramic fibers have become an important commercial material, the EPA promulgated regulations on fiber exposure as negotiated with the ceramic fiber industry to keep exposure below 1.0×10^6 fibers/m^3 [1.0 fibers/cc].

The Consumer Product Safety Commission (CPSC) provides guidance to manufacturers regarding the material content and potential hazards of commercial products. One such product to be targeted was hairdryers, prompting measurements of their emissions (Geraci et al., 1979). Individual state agencies set regulations that are often more stringent than those of the national agencies (Abbott, 1990).

The National Institute for Occupational Safety and Health (NIOSH) recommends health standards to OSHA and MSHA. NIOSH urged elimination, or reduction to the lowest possible levels, of exposures to asbestos fibers and recommended an exposure guideline of 0.1 fiber/cc based on practical limitations of PCM measurements (National Institute for Occupational Safety and Health, 1990).

Regulation of other fibers (e.g., fibrous glass and mineral wool) has generally dealt with these materials as nuisance dust. However, this may change because fibers other than asbestos have been demonstrated to have disease potential in humans and animals. For instance, erionite (a fibrous zeolite) has been associated with human mesotheliomas (Baris, 1980), and several manmade fibers have produced disease in animal exposure studies (Pott et al., 1987; Smith et al., 1987). Refractory ceramic fibers have produced mesothelioma in animals, and nylon fibers have produced acute inflammatory reactions in the lungs of rats (Porter et al., 1999) and humans (Jones et al., 1998).

Asbestos Terminology

Asbestos is a term applied to several commercial minerals exploited for their useful properties, largely due to their tendency to produce long, thin fibers. The development of asbestos crystal structure occurs primarily along one crystal axis. This results in a structure consisting of fibrils (the smallest diameter fibers, 0.025 to 0.05 μm diameter) bundled together. When subjected to comminution, asbestos normally breaks down into particles (fibers) that have high aspect ratios on both macroscopic and microscopic scales; the mineralogical term for

this condition is *asbestiform* (American Society for Testing Materials, 1982). Other minerals with the same chemistry and crystal structure but without the unequal crystal development tend to produce more regular particles (termed *cleavage fragments*), though some of these particles also may be elongated. Although these cleavage fragments have a length/width distribution different from the asbestiform fibers (Virta et al., 1983), individual elongated cleavage fragments are often indistinguishable from asbestiform fibers when measured with commonly available techniques.

The asbestiform minerals that have been regulated include the following six: chrysotile (serpentine), amosite (cummingtonite-grunerite), crocidolite (glaucophane-riebeckite), tremolite asbestos, actinolite asbestos, and anthophyllite asbestos. The nonasbestiform mineral names for the first three materials are provided in parentheses. The latter three have the term *asbestos* attached because nonasbestiform varieties of these minerals have the same name. The latter five types of asbestos are classified as amphiboles. There are other asbestiform or fibrous minerals, but these are relatively rare and, except for attapulgite and wollastonite, have not been exploited commercially (Zumwalde and Dement, 1977). Richterite, or soda-tremolite, is similar to tremolite except that calcium in the crystal structure is replaced with sodium. It has been found as a contaminant of some vermiculite.

Health-related regulations, based on available microscope measurement methods, have specified asbestos fibers as particles with the elemental composition (from X-ray analysis) and crystal structure (from electron diffraction) appropriate to asbestos and with a length greater than 5 μm and an aspect ratio greater than 3:1 (Occupational Safety and Health Administration, 1986; National Institute for Occupational Safety and Health, 1990). Thus, the health-related regulatory definitions of asbestos fibers are based on measurements that may include particles that are cleavage fragments and not necessarily asbestiform. This definition is in contrast to the mineralogical definition relating to the asbestiform crystal structure, which often produces particle distributions with higher mean aspect ratios (Wylie, 1979; Kelse and Thompson, 1989).

The term *asbestos structure* is used for reporting asbestos air concentration under the Asbestos Hazard Emergency Relief Act (AHERA) regulations (Environmental Protection Agency, 1987). An asbestos structure is any particle (fiber, bundle, cluster, or matrix) consisting of or containing an observed fiber segment. This fiber segment must be longer than 0.5 μm with an aspect ratio of 5:1 or greater and be identified as asbestos by elemental analysis and electron diffraction. This definition is used to provide a sensitive method for assessing cleanliness after asbestos removal has been completed.

Measurement Techniques

Sampling and Measurement. There are two main classes of measurement techniques for fibers: microscopic observation of individual fibers and light-scattering–based instruments. Other instruments described in this book also can detect fiber aerosols, but, because they are not specific for fibers, are not considered here. Microscopic techniques require the collection of samples, most often filter samples, that are returned to the laboratory for preparation and analysis by a microscopist. Sample collection is most often carried out using a 25 mm diameter conductive plastic cassette with a 50 mm long inlet (cowl) to prevent direct deposition or contamination of the filter surface. The sampler provides some measure of size selection of collected fibers that varies with sampling rate and environmental conditions (Chen and Baron, 1996). Fiber sampling with a classifying inlet has been proposed to remove fibers and other particles not likely to deposit in the lungs (Baron, 1996).

Four principle types of microscopes are used for fiber detection and analysis: the phase contrast light microscope (PCM), the polarized light microscope (PLM), the scanning electron microscope (SEM), and the transmission electron microscope (TEM). A review of microscope techniques for workplace and environmental asbestos measurements is given by

Chatfield (1986). Descriptions of various light and electron microscopic techniques as well as pictures of many different types of fibers and particles are given in the seven volume *Particle Atlas* (McCrone and Delly, 1973). Other techniques described in Chapter 12 have also been used to analyze fibers.

Sample analysis can take place at various levels of complexity, for example, counting fibers having dimensions within prescribed size limits; determining the fiber size distribution; and measurement of the complete size distribution as well as qualitative analysis of individual fibers. The first is usually applied to establish compliance with regulations and may require some qualitative analysis as well as simple counting of fibers. The latter types of analysis are usually reserved for research studies or environmental assessments where fiber sources are unknown.

Sample preparation is extremely important for microscopic analysis because the view of the fibers and other particles is largely two-dimensional and only a small fraction of the sample is actually observed. Thus, the particles must be uniformly distributed at optimum concentration or loading over the sample surface. If the loading is too high, fibers and particles will overlap and be difficult to analyze; if the loading is too low, it will take too long to find a useful number of fibers (Peck et al., 1986; IARC, 1988). Low filter loading may also cause an overestimate of fiber concentration in some cases because fibers stand out more readily in a clean background (Cherrie et al., 1986).

Phase contrast microscopy is perhaps the most often used technique for monitoring airborne concentrations of asbestos and other fibers in workplace and other environments because it can be accomplished relatively quickly and inexpensively. Cellulose-based filters are used to collect the fibers, and then the filter is chemically cleared on a glass slide. The fibers are observed in a phase contrast microscope at approximately ×450 magnification and counted within observation fields defined by a graticule such as indicated in Figure 23–20. Between 20 and 100 of such fields are normally counted to obtain a statistically meaningful number of fibers (National Institute for Occupational Safety and Health, 1994).

The Environmental Protection Agency (1989) has evaluated asbestos sample preparation techniques. Most analyses of fibrous aerosol samples are performed on filter samples that are prepared without disturbing the location of the fibers on the filter surface (direct transfer sample preparation). This approach has been taken because asbestos fibers can break up when resuspended in a liquid (especially when ultrasonicated), increasing the fiber number. When sampling other fiber types that do not break apart or when sampling problems dictate dilution of the collected sample, a liquid suspension and redeposition of the fibers may be performed (indirect transfer sample preparation). Indirect sample preparation has the advantages of allowing removal of some interfering particles as well as providing a more uniformly deposited sample.

Bulk sample analysis by polarized light microscopy is often used in conjunction with air sampling to find potential sources of airborne fibers. X-ray diffraction (Abell, 1984) and other bulk analysis techniques have also been used for asbestos and other fibers; however, these techniques are not specific for fibers and often are not sufficiently sensitive for aerosol sample analysis. Chapter 12 provides details of these and other analytical techniques that may be applied to asbestos or other fibers.

There have been several attempts to improve the accuracy and speed and to reduce the subjectivity of microscope analysis by using automated image analysis of asbestos fiber samples (Whisnant, 1975). Automated image analysis involves taking the image from a microscope, digitizing the image, and using a computer to evaluate the number and size of objects present in the image. For fiber analysis, this may involve counting the number of fibers present or obtaining a size distribution of the fibers.

An image analysis system was coupled with PCM analysis of asbestos fibers. The Manchester Asbestos Program (MAP) was developed at the Manchester University (U.K.) with

support from the Health and Safety Executive (Kenny, 1984, 1988). The MAP operated in a semiautomated mode, with the analyst selecting fields and focusing the microscope. The MAP was used for a time in various quality assurance programs but did not exhibit sufficient equivalency to human counting for continued use (Baron and Shulman, 1987).

Many image analysis systems are available with simple software for counting larger, well-defined fibers. For instance, they work reasonably well for fibrous glass insulation or synthetic organic textile fibers. Such programs typically have difficulty with asbestos fiber images because of the difficulty of detecting fibers of various diameters and curvatures, some barely visible, some overlapping, in the presence of a noisy image background containing particles of different shapes and sizes. However, with increased computer power and improved image analysis techniques, more accurate automated fiber counting may be possible in the future. A recently developed asbestos fiber counting program shows promise (Inoue et al., 1998).

Although not a complete image analysis system, Lundgren and co-workers (1995) used a computer display of a PCM microscope image to aid the analyst by recording the fiber count and location of each fiber during the analysis. A similar computer-based display system was coupled to a polarizing light microscope and used for quantitative measurement of tremolite fibers in dolomite (Lundgren et al., 1996).

Direct-Reading Fiber Measurement. An optical particle counter has been used for detection of chrysotile fibers in a textile plant where asbestos was the primary aerosol contaminant (Rickards, 1978). Other direct-reading monitors also may be used when the fibers are the major constituent in the aerosol, as in laboratory studies.

A fibrous aerosol monitor was developed for more specific measurement of asbestos fibers in the presence of compact particles (Lilienfeld et al., 1979). This instrument detects fibers via a combined electrostatic alignment/optical scattering technique. A commercial version of the Fibrous Aerosol Monitor (FAM-1, ***MIE***) was produced and has undergone continuous improvement, primarily in ruggedness for field use, over the past 10 years. A more recent version having a data logger and computer control was produced (FM-7400, ***MIE***). See Chapter 18 for more discussion of the FAM-1 and FM-7400 operation principles and evaluations.

Fiber length measurement using light scattering in the FAM was investigated (Cluff and Patitsas, 1992) and indicated good correlation between lengths measured using the FAM and by SEM analysis. A dielectrophoresis-based fiber length classifier was combined with an aerodynamic sizing instrument to obtain a fiber length and diameter distribution in near real time (Baron et al., 2000).

Other direct-reading instruments combining fiber alignment and light scattering have been developed for asbestos monitoring. Rood et al. (1992) developed a technique using fiber alignment by shear forces in an inlet tube, deposition by electrostatic precipitation, and detection by differential light scattering. Another device, the Fibrecheck (***CAS***), measured scattering at multiple angles to differentiate between fibers and compact particles. No field trials of these instruments have been published. All of these devices suffer from similar problems in accurately relating observed fiber counts to the standard approach (i.e., the filter collection/PCM counting method).

A general-purpose light-scattering instrument was developed that uses photomultipliers to detect light scattering in the forward direction and at three azimuthal angles, each gathering light between 27° and 140° from the forward direction. The four scattering values for each particle allowed classification of particles into shape-related groups (Kaye et al., 1996). A commercial version of this instrument is available (***BIR***). Further development of this concept used a detector array to give more complete scattering patterns (Kaye et al., 1992). An extension of the multiangle fiber measurement approach was developed by Sachweh and co-workers (1999). See Chapter 15 for further information about light-scattering instruments.

REFERENCES

Abbott, S. H. 1990. "State regulatory watch." *Asbestos Issues* December:16–25.

Abell, M. T. 1984. Chrysotile asbestos method 9000. In *NIOSH Manual of Analytical Methods*. P. Eller, ed. Cincinnati: National Institute for Occupational Safety and Health.

Allen, M. D. and J. K. Briant. 1978. Characterization of LMFBR fuel sodium aerosols. *Health Phys.* 35(2):237–254.

Allen, M. D., J. K. Briant, and O. R. Moss. 1979. Comparison of the aerodynamic size distribution of chain-like aggregates measured with a cascade impactor and a spiral centrifuge. *Am. Ind. Hyg. Assoc. J.* 40:474–481.

Allen, M. D., O. R. Moss, and J. K. Briant. 1978. Dynamic shape factors for LMFBR mixed-oxide fuel aggregates. *J. Aerosol Sci.* 10:43–48.

American Society for Testing Materials. 1982. Safety and health requirements relating to occupational exposure to asbestos. E 849-82. American Society for Testing Materials.

Asgharian, B. and M. N. Godo. 1999. Size separation of spherical particles and fibers in an aerosol centrifuge. *Aerosol Sci. Technol.* 30(4):383–400.

Asgharian, B. and C. P. Yu. 1988. Deposition of inhaled fibrous particles in the human lung. *J. Aerosol Med.* 1(1):37–50.

Asgharian, B. and C. P. Yu. 1989. A simplified model of interceptional deposition of fibers at airway bifurcations. *Aerosol Sci. Technol.* 11:80–88.

Asgharian, B., L. Zhang, and C. P. Fang. 1997. Theoretical calculations of the collection efficiency of spherical particles and fibers in an impactor. *Aerosol Sci. Technol.* 28:277–287.

Balásházy, I., T. B. Martonen, and W. Hofmann. 1990. Fiber deposition in airway bifurcations. *J. Aerosol Med.* 3:243–260.

Baris, Y. 1980. The clinical and radiological aspects of 185 cases of malignant pleural mesothelioma, ed. J. C. Wagner. *Biological Effects of Mineral Fibres*, Vol. 2. Lyon: International Agency for Research on Cancer, pp. 937–947.

Baron, P. A. 1996. Application of the thoracic sampling definition to fiber measurement. *Am. Ind. Hyg. Assoc. J.* 57:820–824.

Baron, P. A. and G. J. Deye. 1987. Generation of replicate asbestos aerosol samples for quality assurance. *Appl. Ind. Hyg.* 2:114–118.

Baron, P. A. and G. J. Deye. 1990. Electrostatic effects in asbestos sampling I: Experimental measurements. *Am. Ind. Hyg. Assoc. J.* 51:51–62.

Baron, P. A., G. J. Deye, and J. Fernback. 1994. Length separation of fibers. *Aerosol Sci. Technol.* 21: 179–192.

Baron, P. A., G. J. Deye, J. E. Fernback, and W. G. Jones. 2000. Direct-reading measurement of fiber length/diameter distributions, eds. M. E. Beard and H. L. Rook. *Advances in Environmental Measurement Methods for Asbestos*. Boulder, CO: American Society for Testing Materials, STP 1342.

Baron, P. A., P. Gao, G. J. Deye, and A. C. Maynard. 1998. Performance of a fiber length classifier. *J. Aerosol Sci.* 29(Suppl. 1):S11–S12.

Baron, P. A. and S. A. Shulman. 1987. Evaluation of the Magiscan image analyzer for asbestos fiber counting. *Am. Ind. Hyg. Assoc. J.* 48:39–46.

Bellmann, B., H. König, H. Muhle, and F. Pott. 1986. Chemical durability of asbestos and of man-made mineral fibres in vivo. *J. Aerosol Sci.* 17:341–345.

Blake, T., V. Castranova, D. Schwegler-Berry, G. J. Deye, P. Baron, C. Li, and W. Jones. 1997. Effect of fiber length on glass microfiber cytotoxicity. *J. Tox. Environ. Health* 54A:243–259.

Brockmann, J. E. 1985. Appendix F. *Uncertainty in Radionuclide Release Under Specific LWR Accident Conditions*. Albuquerque, NM: Sandia National Laboratories, SAND84-0410, Vol. 2.

Brockmann, J. E. 1987. Ex-vessel releases: Aerosol source terms in reactor accidents. *Prog. Nucl. Energy* 19:7–68.

Brockmann, J. E. and D. J. Rader. 1990. APS response to nonspherical particles and experimental determination of dynamic shape factor. *Aerosol Sci. Technol.* 13:162–172.

Burke, W. A. and N. A. Esmen. 1978. The inertial behavior of fibers. *Am. Ind. Hyg. Assoc. J.* 39:400–405.

Cai, J., N. Lu, and C. M. Sorensen. 1993. Comparison of size and morphology of soot aggregates as determined by light scattering and electron microscope analysis. *Langmuir* 9:2861–2068.

Cai, J., N. Lu, and C. M. Sorensen. 1995a. Analysis of fractal cluster morphology parameters: Structural coefficient and density autocorrelation function cutoff. *J. Colloid Interface Sci.* 171:470–473.

Cai, J., N. Lu, and C. M. Sorensen. 1995b. Fractal cluster size distribution measurement using static light scattering. *J. Colloid Interface Sci.* 174:456–460.

Cai, J. and C. M. Sorensen. 1994. Diffusion of fractal aggregates in the free molecular regime. *Phys. Rev. E.* 50:3397–3401.

Carpenter, R. L., J. A. Pickrell, B. V. Mokler, H. C. Yeh, and P. B. DeNee. 1981. Generation of respirable glass fiber aerosols using a fluidized bed aerosol generator. *Am. Ind. Hyg. Assoc. J.* 42:777–784.

Chan, P. and B. Dahneke. 1981. Free-molecular drag on straight chains of uniform spheres. *J. Appl. Phys.* 52:3106.

Chatfield, E. J. 1986. Asbestos measurements in workplaces and ambient atmospheres, eds. S. Basu and J. R. Millette. *Electron Microscopy in Forensic, Occupational and Environmental Health Sciences*. New York: Plenum Publishing Corp.

Chen, C.-C. and P. A. Baron. 1996. Aspiration efficiency and wall deposition in the fiber sampling cassette. *Am. Ind. Hyg. Assoc. J.* 52(2):142–152.

Chen, Y. K. and C. P. Yu. 1990. Sedimentation of charged fibers from a two-dimensional channel flow. *Aerosol Sci. Technol.* 12:786–792.

Cheng, M. T., G. W. Xie, M. Yang, and D. T. Shaw. 1991. Experimental characterization of chain-aggregate aerosol by electrooptic scattering. *Aerosol Sci. Technol.* 14(1):74–81.

Cheng, Y.-S. 1986. Bivariate lognormal distribution for characterizing asbestos fiber aerosols. *Aerosol Sci. Technol.* 5(3):359–368.

Cheng, Y.-S., M. D. Allen, D. P. Gallegos, and H.-C. Yeh. 1988. Drag force and slip correction of aggregate aerosols. *Aerosol Sci. Technol.* 8:199–214.

Cherrie, J., A. D. Jones, and A. M. Johnston. 1986. The influence of fiber density on the assessment of fiber concentration using the membrane filter method. *Am. Ind. Hyg. Assoc. J.* 47:465–474.

Chissick, S. S. and R. Derricot. 1983. *Asbestos, Properties, and Applications and Hazards*. Chichester: John Wiley & Sons.

Clift, R., J. R. Grace, and M. E. Weber. 1978. *Bubbles, Drops and Particles*. New York: Academic Press.

Cluff, D. L. and A. J. Patitsas. 1992. Size characterization of asbestos fibers by means of electrostatic alignment and light-scattering techniques. *Aerosol Sci. Technol.* 17(3):186–198.

Cox, R. G. 1970. The motion of long slender bodies in a viscous fluid I: General theory. *J. Fluid Mech.* 44:791.

Craig, D. K., C. A. Lapin, and G. E. Butterfield. 1991. The generation and characterization of silicon carbide whiskers (fibers) for inhalation toxicology studies. *Am. Ind. Hyg. Assoc. J.* 52(8):315–319.

Dahneke, B. 1982. Viscous resistance of straight-chain aggregates of uniform spheres. *Aerosol Sci. Technol.* 1:179–185.

Dahneke, B. E. 1973a. Slip correction factors for nonspherical bodies—I. Introduction and continuum flow. *J. Aerosol Sci.* 4:139–145.

Dahneke, B. E. 1973b. Slip correction factors for nonspherical bodies—II. Free molecule flow. *J. Aerosol Sci.* 4:147–161.

Dahneke, B. E. 1973c. Slip correction factors for nonspherical bodies—III. The form of the general law. *J. Aerosol Sci.* 4:163–170.

Dement, J. M. 1990. Overview: Workshop on fiber toxicology research needs. *Environ. Health Perspect.* 88:261–268.

Dobbins, R. A. and C. M. Magaridis. 1987. Morphology of flame-generated soot as determined by thermophoretic sampling. *Langmuir* 3:254–259.

Environmental Protection Agency. 1985. *Measuring Airborne Asbestos Following an Abatement Action*. EPA 600/4-85-049. EPA 600/4-85-049. Quality Assurance Division, Environmental Protection Agency.

Environmental Protection Agency. 1987. Asbestos-containing materials in schools. *Federal Register 40 CFR Part 763*. Washington, DC: Government Printing Office, April 30, 1987, 40 CFR Part 763.

Environmental Protection Agency. 1989. *Comparison of Airborne Asbestos Levels Determined by Transmission Electron Microscopy (TEM) Using Direct and Indirect Transfer Techniques*. EPA 560/5-89-004. EPA 560/5-89-004. Environmental Protection Agency.

Environmental Protection Agency. 1990. *Managing Asbestos in Place: A Building Owners Guide to Operations and Maintenance Programs for Asbestos Containing Materials*. EPA 20T-2003. EPA 20T-2003. Environmental Protection Agency.

Fairchild, C. I., L. W. Ortiz, H. J. Ettinger, and M. I. Tillery. 1976. *Aerosol Research and Development Related to Health Hazard Analysis*. LA-6277-PR. Los Alamos Scientific Laboratory.

Fairchild, C. I., L. W. Ortiz, M. I. Tillery, and H. J. Ettinger. 1978. *Aerosol Research and Development Related to Health Hazard Analysis*. LA-7380-PR. Los Alamos Scientific Laboratory.

Family, F. 1991. Fractals, eds. R. G. Lerner and G. L. Trigg. *Encyclopedia of Physics*, 2nd ed. New York: VCH Publishers, Inc., p. 414.

Family, F. and D. P. Landau. 1984. *Kinetics of Aggregation and Gelation*. Amsterdam: North-Holland.

Forrest, S. R. and T. A. Witten, Jr. 1979. Long-range correlations in smoke-particle aggregates. *J. Phys. A Math. Gen.* 12:L109–L117.

Frazer, D. G., V. Robinson, K. Jayaraman, K. C. Weber, D. S. DeLong, and C. Glance. 1986. *Improved Operating Parameters for the Pitt 3 Aerosol Generator During Resuspension of Respirable Cotton Dust*. The Tenth Cotton Dust Research Conference, National Cotton Council, Memphis, TN.

Friedlander, S. K., H. D. Jang, and K. H. Ryu. 1998. Elastic behavior of nanoparticle chain aggregates. *Appl. Phys. Lett.* 72:173–175.

Fu, T.-H., M.-T. Cheng, and D. Shaw. 1990. Filtration of chain aggregate aerosols by model screen filter. *Aerosol Sci. Technol.* 13(2):151–161.

Fuchs, N. A. 1964. *The Mechanics of Aerosols*. Oxford: Pergamon Press.

Gallily, I. 1971. On the drag experienced by a spheroidal, small particle in a gravitational and electrostatic field. *J. Colloid Interface Sci.* 36(3):325–339.

Gallily, I. and A. D. Eisner. 1979. On the orderly nature of the motion of nonspherical aerosol particles I. Deposition from a laminar flow. *J. Colloid Interface Sci.* 68:320–337.

Gallily, I., D. Schiby, A. H. Cohen, W. Holländer, D. Schless, and W. Stöber. 1986. On the inertial separation of nonspherical aerosol particles from laminar flows. I. The cylindrical case. *Aerosol Sci. Technol.* 5(2):267–286.

Gangopadhyay, S., I. Elminyawi, and C. M. Sorensen. 1991. Optical structure factor measurements of soot particles in a premixed flame. *Appl. Opt.* 30(4859–4864).

Gelbard, F. 1982. *MAEROS User Manual*. NUREG/CR-1391 SAND80-0822. Sandia National Laboratories.

Gentry, J. W., K. R. Spurny, J. Schörmann, and H. Opiela. 1983. Measurement of the diffusion coefficient of asbestos fibers, eds. V. A. Marple and B. Y. H. Liu. *Aerosols in the Mining and Industrial Work Environments*. Ann Arbor: Ann Arbor Science Publishers. 2:597–612.

Gentry, J. W., K. R. Spurny, S. A. Soulen, and J. Schörmann. 1988. Measurements of the diffusion coefficients of ultrafine asbestos fibers. *J. Aerosol Sci.* 19(7):1041–1044.

Geraci, C., P. A. Baron, J. W. Carter, and D. L. Smith. 1979. *Testing of Hair Dryer Emissions*, IA-79-29. National Institute for Occupational Safety and Health.

Gieseke, J. A., L. D. Reed, H. Jordan, and K. W. Lee. 1977. *Characteristics of Agglomerates of Sodium Oxide Aerosols*. BMI-NUREG-1977 NRC-7. Columbus, OH: Battelle Columbus Laboratories.

Gonda, I. and A. F. A. E. Khalik. 1985. On the calculation of aerodynamic diameters of fibers. *Aerosol Sci. Technol.* 4:233–238.

Griffis, L. C., J. A. Pickrell, R. L. Carpenter, R. K. Wolff, S. J. McAllen, and K. L. Yerkes. 1983. Deposition of crocidolite asbestos and glass microfibers inhaled by the beagle dog. *Am. Ind. Hyg. Assoc. J.* 44(3):216–222.

Griffiths, W. D., L. C. Kenny, and S. T. Chase. 1985. The electrostatic separation of fibres and compact particles. *Ann. Occup. Hyg.* 16(3):229–243.

Griffiths, W. D. and N. P. Vaughan. 1986. The aerodynamic behaviour of cylindrical and spheroidal particles when settling under gravity. *J. Aerosol Sci.* 17(1):53–65.

Guinier, A., G. Fournet, C. B. Walker, and K. L. Yudowitch. 1955. *Small Angle Scattering of X-Rays*. New York: John Wiley & Sons.

Hanton, D. Y., H. Furtak, and H. G. Grimm. 1998. Preparation and handling conditions of MMVF for in-vivo experiments. *Aerosol Sci. Technol.* 29:449–456.

Helton, J. C., R. L. Iman, J. D. Johnson, and C. D. Leigh. 1986. *Uncertainty and Sensitivity Analysis of a Dry Containment Test Problem for the MAEROS Aerosol Model*. SAND85-2795. Sandia National Laboratories.

Hinds, W. C. 1999. *Aerosol Technology*. New York: John Wiley & Sons.

Holst, E. and T. Schneider. 1985. Fibre size characterization and size analysis using general and bivariate log-normal distributions. *J. Aerosol Sci.* 5:407–413.

Holt, P. F. 1987. *Dust and Disease*. New York: John Wiley & Sons.

IARC. 1988. Man-Made Mineral Fibers and Radon. *IARC Monographs of the Evaluation of the Carcionogenic Risk of Chemicals in Humans*. Lyon, France: International Agency for Research on Cancer, pp. 33–171.

Iles, P. J. 1990. Size selection of fibres by cyclone and horizontal elutriator. *J. Aerosol Sci.* 21(6):745–760.

Inoue, Y., A. Kaga, K. Yamaguchi, and S. Kamoi. 1998. Development of an automatic system for counting asbestos fibers using image processing. *Part. Sci. Technol.* 16:263–279.

Johnson, D. L., D. Leith, and P. C. Reist. 1987. Drag on non-spherical orthotropic aerosol particles. *J. Aerosol Sci.* 18(1):87–97.

Johnson, N. F., D. M. Griffiths, and R. J. Hill. 1984. Size distribution following long term inhalation of MMMF. *Biological Effects of Man-Made Mineral Fibers*, Vol. 2. Copenhagen: World Health Organization, pp. 102–125.

Johnston, A. M., J. H. Vincent, and A. D. Jones. 1985. Measurements of electric charge for workplace aerosols. *Ann. Occup. Hyg.* 29(2):271–284.

Jones, A. D., A. M. Johnston, and J. H. Vincent. 1983. Static electrification of airborne asbestos dust, eds. V. A. Marple and B. Y. H. Liu. *Aerosols in the Mining and Industrial Work Environment*, Vol. 2. Ann Arbor, MI: Ann Arbor Science, pp. 613–632.

Jones, W. G., C. Piacitelli, D. Schwegler-Berry, and J. Burkhart. 1998. *Environmental Study of Nylon Flocking Process*. NIOSH.

Jullien, R., R. Thouy, and F. Ehrburger-Doll. 1994. Numerical investigation of two-dimensional projections of random fractal aggregates. *Phys. Rev.* E50:3878–3882.

Kasper, G. 1982. Dynamics and measurement of smokes. II. The aerodynamic diameter of chain aggregates in the transition regime. *Aerosol Sci. Technol.* 1(2):201–216.

Kasper, G. 1983. Note on the slip coefficient of doublets of spheres. *J. Aerosol Sci.* 14(6):753–754.

Kasper, G. and D. T. Shaw. 1983. Comparative size distribution measurements on chain aggregates. *Aerosol Sci. Technol.* 2:369–381.

Kasper, G., S. N. Shon, and D. T. Shaw. 1980. Controlled formation of chain aggregates from very small metal oxide particles. *Am. Ind. Hyg. Assoc. J.* 41:288–296.

Kaye, P. H., K. Alexander-Buckley, E. Hirst, et al. 1996. A real-time monitorng system for airborne particle shape and size analysis. *J. Geophys. Res.* 101:19215–19221.

Kaye, P. H., E. Hirst, J. M. Clark, and F. Micheli. 1992. Airborne particle shape and size classification from spatial light scattering profiles. *J. Aerosol Sci.* 23(6):597–612.

Kelse, J. W. and C. S. Thompson. 1989. The regulatory and mineralogical definitions of asbestos and their impact on amphibole dust analysis. *Am. Ind. Hyg. Assoc. J.* 50:613–622.

Kenny, L. C. 1984. Asbestos fibre counting by image analysis—The performance of the Manchester Asbestos Program on Magiscan. *Ann. Occup. Hyg.* 28:401–415.

Kenny, L. C. 1988. Automated analysis of asbestos clearance samples. *Ann. Occup. Hyg.* 32(1):115–128.

Kerker, M. 1969. *The Scattering of Light and Other Electromagnetic Radiation*. New York: Academic Press.

Kolb, M., R. Botet, and R. Jullien. 1983. Scaling of kinetically growing clusters. *Phys. Rev. Lett.* 51: 1123–1126.

Kops, J., G. Dibbets, L. Hermans, and J. F. Van der Vate. 1975. The aerodynamic diameter of branched chain-like aggregates. *J. Aerosol Sci.* 6(5):329–334.

Köylü, U. O. and G. M. Faeth. 1992. Structure of overfire soot in buoyant turbulent diffusion flames at long residence times. *Combust. Flame* 89:140–156.

Köylü, U. O., G. M. Faeth, T. L. Farias, and M. G. Carvalho. 1995. Fractal and projected structure properties of soot aggregates. *Combust. Flame* 100:621–633.

Laframboise, J. G. and J.-S. Chang. 1977. Theory of charge deposition on charged aerosol particles of arbitrary shape. *J. Aerosol Sci.* 8:331–338.

Langer, A. 1974. The subject of continuous vigilance. *Environ. Health Perspect.* 9:53–56.

Langer, A. M., A. D. Mackler, and F. D. Pooley. 1974. Electron microscopical investigation of asbestos fibers. *Environ. Health Perspect.* 9:63–80.

Law, B. D., W. B. Bunn, and T. W. Hesterburg. 1990. Solubility of polymeric organic fibers and manmade vitreous fibers in gambles solution. *Inhal. Toxicol.* 2:321–339.

Light, W. G. and E. T. Wei. 1977. Surface charge and asbestos toxicity. *Science* 265:537–539.

Lilienfeld, P. 1985. Rotational electrodynamics of airborne fibers. *J. Aerosol Sci.* 16(4):315–322.

Lilienfeld, P., P. Elterman, and P. Baron. 1979. Development of a prototype fibrous aerosol monitor. *Am. Ind. Hyg. Assoc. J.* 40(4):270–282.

Lin, M. Y., H. M. Lindsay, D. A. Weitz, R. C. Ball, R. Klein, and P. Meakin. 1990. Universal reaction-limited colloid aggregation. *Phys. Rev. A* 41:2005–2020.

Lipowicz, P. J. and H. C. Yeh. 1989. Fiber dielectrophoresis. *Aerosol Sci. Technol.* 11:206–212.

Lippmann, M. 1988. Asbestos exposure indices. *Environ. Res.* 46:86–106.

Lundgren, L., S. Lundström, I. Laszlo, and B. Westling. 1995. Modern fibre counting—A technique with the phase-contrast microscope on-line to a Macintosh computer. *Ann. Occup. Hyg.* 39(4):455–467.

Lundgren, L., S. Lundström, G. Sundström, G. Bergman, and S. Krantz. 1996. A quantitative method using a light microscope on-line to a Macintosh computer for the analysis of tremolite fibres in dolomite. *Ann. Occup. Hyg.* 40:197–209.

Mandelbrot, B. B. 1977. *Fractals: Form, Chance and Dimension*. San Francisco: W. H. Freeman.

Mandelbrot, B. B. 1983. *The Fractal Geometry of Nature*. New York: W. H. Freeman and Company.

Martin, J. E. and B. J. Ackerson. 1985. *Phys. Rev. A* 31:1180–1182.

Martonen, T. B. and D. L. Johnson. 1990. Aerodynamic classification of fibers with aerosol centrifuges. *Part. Sci. Technol.* 8:37–53.

McCrone, W. C. and J. G. Delly. 1973. *The Particle Atlas*. Ann Arbor, MI: Ann Arbor Science Publishers, Inc.

Meakin, P. 1983. Formation of fractal clusters and networks by irreversible diffusion-limited aggregation. *Phys. Rev. Lett.* 51:1119–1122.

Meakin, P. 1984. Effects of cluster trajectories on cluster-cluster aggregations: A comparison of linear and brownian trajectories in two- and three-dimensional simulations. *Phys. Rev. A* 29:997–999.

Meakin, P. 1988. Fractal aggregates. *Adv. Colloid Interface Sci.* 28:249–331.

Meakin, P., B. Donn, and G. W. Mulholland. 1989. Collisions between point masses and fractal aggregates. *Langmuir* 5:510–518.

Medalia, A. I. 1967. Morphology of aggregates. *J. Colloid Interface Sci.* 24:393–404.

Medalia, A. I. and F. A. Heckman. 1969. Morphology of aggregates—II. Size and shape factors of carbon black aggregates from electron microscopy. *Carbon* 7:567–582.

Megaridis, C. M. and R. A. Dobbins. 1990. Morphological description of flame generated materials. *Combust. Sci. Technol.* 71:95–109.

Michaels, L. and S. S. Chissick. 1979. *Asbestos: Properties, Applications and Hazards*. Chichester: John Wiley & Sons.

Mine Safety and Health Administration. 1988. *Exposure Limits for Airborne Contaminants*. CFR Part 56.5001. Washington, DC: U.S. Department of Commerce.

National Institute for Occupational Safety and Health. 1976. *Revised Recommended Asbestos Standard.* Publ. (NIOSH) 77–169. Cincinnati: U.S. Department of Health Education and Welfare.

National Institute for Occupational Safety and Health. 1977. *Occupational Exposure to Fibrous Glass.* DHEW (NIOSH) Publication No. 77–152. Cincinnati: National Institute for Occupational Safety and Health.

National Institute for Occupational Safety and Health. 1990. *Testimony of NIOSH on Occupational Exposure to Asbestos, Tremolite, Anthophyllite an Actinolite.* 29CFR Parts 1910 and 1926. Cincinnati: National Institute of Occupational Safety and Health.

National Institute for Occupational Safety and Health. 1994. *Asbestos and Other Fibers by PCM.* Method 7400. *NIOSH Manual of Analytical Methods*, 4th ed. Cincinnati: National Institute for Occupational Safety and Health.

Occupational Safety and Health Administration. 1986. *Occupational Exposure to Asbestos, Tremolite, Anthophyllite, and Actinolite Asbestos; Final Rules.* 29 CFR Part 1910.1001 and 1926. Washington, DC: Occupational Safety and Health Administration.

Oh, C. and C. M. Sorensen. 1997. The effect of monomer overlap on the morphology of fractal aggregates. *J. Colloid. Interface Sci.* 193:17–25.

Oh, C. and C. M. Sorensen. 1998. Structure factor of diffusion-limited aggregation clusters: Local structure and non-self-similarity. *Phys. Rev. E* 57:784–790.

Oh, C. and C. M. Sorensen. 1999. Scaling approach for the structure factor of a generalized system of scatterers. *J. Nanopart. Res.* 1:369–377.

Peck, A. S., J. J. Serocki, and L. C. Dicker. 1986. Sample density and the quantitative capabilities of PCM analysis for the measurement of airborne asbestos. *Am. Ind. Hyg. Assoc. J.* 47:A230–A234.

Porter, D. W., V. Castranova, R. A. Robinson, A. F. Hubbs, R. R. Mercer, J. Scabilloni, T. Goldsmith, D. Schwegler-Berry, L. Battelli, et al. 1999. Acute inflammatory reaction in rats after intratracheal instillation of material collected from a nylon flocking plant. *J. Toxicol. Environ. Health.* Part A 57:25–45.

Pott, F. 1978. Some aspects on the dosimetry of the carcinogenic potency of asbestos and other fibrous dusts. *Staub Rein. Luft* 38:486.

Pott, F., U. Ziem, F. J. Reiffer, F. Huth, H. Ernst, and U. Mohr. 1987. Carcinogenicity studies of fibers, metal compounds, and some other dusts in rats. *Exp. Pathol.* 32:129–152.

Prenni, A. J., R. L. Siefert, T. B. Onasch, and M. A. Tolbert. 2000. Design and characterization of a fluidized bed aerosol generator: A source for dry, submicrometer aerosol. *Aerosol Sci. Technol.* 32(5):465–481.

Prodi, V., T. De Zaiocomo, D. Hochrainer, and K. Spurny. 1982. Fibre collection and measurement with the inertial spectrometer. *J. Aerosol Sci.* 13:49–58.

Rajhans, G. S. and J. L. Sullivan. 1981. *Asbestos Sampling and Analysis.* Ann Arbor, MI: Ann Arbor Science Publishers.

Ren, Z. F., Z. P. Huang, J. W. Xu, J. H. Wang, P. Bush, M. P. Siegal, and P. N. Provencio. 1998. Synthesis of large arrays of well-aligned carbon nanotubes on glass. *Science* 282:1105–1107.

Rickards, A. L. 1978. The routine monitoring of airborne asbestos in an occupational environment. *Ann. Occup. Hyg.* 21:315–322.

Rogak, S. N., U. Baltensperger, and R. C. Flagan. 1990. Direct measurement of mass transfer to agglomerates in the transition regime. *J. Aerosol Sci.* 21(Suppl. 1):S51–S55.

Rood, A. P., E. J. Walker, and D. Moore. 1992. Construction of a portable fiber monitor measuring the differential light scattering from aligned fibres. *Aerosol Sci. Technol.* 17(1):1–8.

Rosner, D. E., D. W. Mackowski, and P. Garcia-Ybana. 1991. Size- and structure-insensitivity of the thermophoretic transport of aggregated soot particles in gases. *Combust. Sci. Tech.* 80:87–101.

Sachweh, B., H. Barthel, R. Polke, H. Umhauer, and H. Buttner. 1999. Particle shape and structure analysis from the spatial intensity pattern of scattered light using different measuring devices. *J. Aerosol Sci.* 30(10):1257–1270.

Sampson, R. J., G. W. Mulholland, and J. W. Gentry. 1987. Structural analysis of soot agglomerates. *Langmuir* 3:272–281.

Schmidt-Ott, A. 1988. In situ measurement of the fractal dimensionality of ultrafine aerosol particles. *Appl. Phys. Lett.* 52:954.

Schneider, T., E. Holst, and J. Skotte. 1983. Size distribution of airborne fibres generated from man-made mineral fiber products. *Ann. Occup. Hyg.* 27(2):157–171.

Selikoff, I. J. and E. C. Hammond. 1979. *Health Hazards of Asbestos Exposure*. New York: New York Academy of Sciences.

Smith, D. M., L. W. Ortiz, and R. F. Archuleta. 1987. Long-term health effects in hamsters and rats exposed to man-made vitreous fibers. *Ann. Occup. Hyg.* 31(4B):731–754.

Sorensen, C. M. 1997. Scattering and absorption of light by particles and aggregates, ed. K. S. Birdi. *Handbook of Surface and Colloid Chemistry*. Boca Raton, FL: CRC Press, pp. 533–558.

Sorensen, C. M. 2001. Light scattering from fractal aggregates. A review. *Aerosol Sci. Technol.* In Press.

Sorensen, C. M., J. Cai, and N. Lu. 1992a. Light-scattering measurements of monomer size, monomers per aggregate, and fractal dimension for soot aggregates in flames. *Appl. Opt.* 31:6547–6557.

Sorensen, C. M., J. Cai, and N. Lu. 1992b. Test of static structure factors for describing light scattering from fractal soot aggregates. *Langmuir* 8:2064–2069.

Sorensen, C. M. and G. D. Feke. 1996. The morphology of macroscopic soot. *Aerosol Sci. Technol.* 25(3):328–337.

Sorensen, C. M., W. B. Hageman, T. J. Rush, H. Huang, and C. Oh. 1998. Aerogelation in a flame soot aerosol. *Phys. Rev. Lett.* 80:1782–1785.

Sorensen, C. M. and G. C. Roberts. 1997. The prefactor of fractal aggregates. *J. Colloid Interface Sci.* 186:447–452.

Sorensen, C. M. and G. M. Wang. 1999. Size distribution effect on the power law regime of the structure factor of fractal aggregates. *Phys. Rev. E* Part B 60:7143–7148.

Spurny, K., C. Boose, and D. Hochrainer. 1975. Zur zerstäubung von asbestfasern in einem fliessbett-aerosolgenerator. *Staub Rein. Luft* 35(12):440–445.

Spurny, K. R. 1980. Fiber generation and length classification, ed. K. Willeke. *Generation of Aerosols and Facilities for Exposure Experiments*. Ann Arbor: Ann Arbor Science Publishers, pp. 257–298.

Stöber, W. 1971. A note on the aerodynamic diameter and the mobility of non-spherical aerosol particles. *J. Aerosol Sci.* 2(4):453–456.

Stöber, W. 1972. Dynamic shape factors of nonspherical aerosol particles, eds. T. T. Mercer, P. E. Morrow, and W. Stöber. *Assessment of Airborne Particles*. Springfield, IL: Charles C. Thomas, pp. 249–289.

Stöber, W., H. Flachsbart, and D. Hochrainer. 1970. The aerodynamic diameter of latex aggregates and asbestos fibers. *Staub Rein. Luft* 30(7):1–12.

Sussman, R. G., J. M. Gearhart, and M. Lippmann. 1985. A variable feed rate mechanism for fluidized bed asbestos generators. *Am. Ind. Hyg. Assoc. J.* 46(1):24–27.

Tanaka, I. and T. Akiyama. 1984. A new dust generator for inhalation toxicity studies. *Ann. Occup. Hyg.* 28(2):157–162.

Tanaka, I. and T. Akiyama. 1987. Fibrous particles generator for inhalation toxicity studies. *Ann. Occup. Hyg.* 31:401–403.

Tanford, C. 1961. *Physical Chemistry of Macromolecules*. New York: John Wiley & Sons.

Timbrell, V. 1972. Alignment of carbon and other man-made fibers by magnetic fields. *J. Appl. Phys.* 43:4839–4840.

Timbrell, V. 1973. *Desired Characteristics of Fibres for Biological Experiments*. Montreal, Canada: Institute of Occupational and Environmental Health.

Timbrell, V. 1975. Alignment of respirable asbestos fibres by magnetic fields. *Ann. Occup. Hyg.* 18: 299–311.

Timbrell, V. 1982. Deposition and retention of fibres in the human lung. *Ann. Occup. Hyg.* 26:347–369.

Timbrell, V. 1989. Review of the significance of fibre size in fibre-related lung disease: A centrifuge cell for preparing accurate microscope-evaluation specimens from slurries used in inoculation studies. *Ann. Occup. Hyg.* 33:483–505.

Timbrell, V., J. C. Gilson, and I. Webster. 1968a. UICC standard reference samples of asbestos. *Int. J. Cancer* 3:406–408.

Timbrell, V, A. W. Hyatt, and J. W. Skidmore. 1968b. A simple dispenser for generating dust clouds from standard reference samples of asbestos. *Ann. Occup. Hyg.* 11:273–281.

Tolles, W. M., R. A. Sanders, and G. W. Fritz. 1974. Dielectric response of anisotropic polarized particles observed with microwaves: A new method for characterizing the properties of nonspherical particles in suspension. *J. Appl. Phys.* 45(9):3777–3783.

Van de Hulst, H. C. 1957. *Light Scattering by Small Particles*. New York: John Wiley & Sons.

van de Vate, J. F., W. F. van Leeuwen, A. Plomp, and H. C. D. Smit. 1980. Dynamic shape factors: Measurement techniques and results on aggregates of solid primaries. *J. Aerosol Sci.* 11:67–75.

Virta, R. L., K. B. Shedd, A. G. Wylie, and J. G. Snyder. 1983. Size and shape characteristics of amphibole asbestos (amosite) and amphibole cleavage fragments (actinolite, cummingtonite) collected on occupational air monitoring filters. In *Aerosols in the Mining and Industrial Work Environments*, V. A. Marple and B. Y. H. Liu, eds. Vol. 2. Ann Arbor: Ann Arbor Science.

Viscek, T. 1992. *Fractal Growth Phenomena*. San Francisco: World Scientific.

Walton, W. H. 1982. The nature, hazards, and assessment of occupational exposure to airborne asbestos dust: A review. *Ann. Occup. Hyg.* 25:115–247.

Wang, G. M. and C. M. Sorensen. 1999. Diffusive mobility of fractal aggregates over the entire Knudsen number range. *Phys. Rev. E* 60:3036.

Wegrzyn, J. and D. T. Shaw. 1979. *NUREG/CR-0799*. Nuclear Regulatory Commission.

Weiss, M. A., A.-H. Cohen, and I. Gallily. 1978. On the stochastic nature of the motion of nonspherical aerosol particles. II. The overall drift angle in sedimentation. *J. Aerosol Sci.* 9:527–541.

Wen, H. Y., G. P. Reischl, and G. Kasper. 1984. Bipolar diffusion charging of fibrous aerosol particles—I. Charging theory. *J. Aerosol Sci.* 15(2):89–101.

Weyel, D. A., M. Ellakkani, Y. Alarie, and M. Karol. 1984. An aerosol generator for the resuspension of cotton dust. *Toxicol. Appl. Pharmacol.* 76:544–547.

Whisnant, R. A. 1975. *Evaluation of Image Analysis Equipment Applied to Asbestos Fiber Counting*. 210-75-0080/5. Cincinnati: National Institute for Occupational Safety and Health.

Wiltzius, P. 1987. Hydrodynamic behavior of fractal aggregates. *Phys. Rev. Lett.* 58:710.

Witten, T. A., Jr. and L. M. Sander. 1981. Diffusion-limited aggregation, a kinetic critical phenomena. *Phys. Rev. Lett.* 47:1400–1403.

Wu, M. K. and S. K. Friedlander. 1993. Note on the powerlaw equation for fractal-like aerosol agglomerates. *J. Colloid Interface Sci.* 159:246–247.

Wylie, A. G. 1979. Fiber length and aspect ratio of some selected asbestos samples. *Ann. NY Acad. Sci.* 330:605–610.

Ye, J., X. Shi, W. Jones, Y. Rojanasakul, N. Cheng, D. Schwegler-Berry, P. A. Baron, G. J. Deye, C. Li, et al. 1999. Critical role of glass fiber length in TNF-α production and transcription factor activation in macrophages. *Am. J. Physiol. Lung C.* 276(March [3 Pat. 1]):L426–L434.

Yu, P. Y., C. C. Wang, and J. W. Gentry. 1987. Experimental measurement of the rate of unipolar charging of actinolite fibers. *J. Aerosol Sci.* 18(1):73–85.

Zhang, H. X., C. M. Sorensen, E. R. Ramer, B. J. Olivier, and J. F. Merklin. 1988. In situ optical structure factor measurements of an aggregating soot aerosol. *Langmuir* 4:867–871.

Zimm, B. H. 1948. Apparatus and methods for measurement and interpretation of the angular variation of light-scattering, preliminary results on polystyrene solutions. *J. Chem. Phys.* 16:1099–1116.

Zumwalde, R. D. and J. M. Dement. 1977. *Review and Evaluation of Analytical Methods for Environmental Studies of Fibrous Particulate Exposures*. DHEW (NIOSH) Publication No. 77-204. Cincinnati: National Institute for Occupational Safety and Health.

00003561331 - 12-28-01 - $95.00 - Corp. Book Resources

AEROSOL MEASUREMENT

Principles, Techniques, and Applications

SECOND EDITION

Edited by

Paul A. Baron, Ph.D.
Physical Scientist
Centers for Disease Control and Prevention
National Institute for Occupational Safety and Health
Cincinnati, OH

Klaus Willeke, Ph.D.
Professor
Department of Environmental Health
University of Cincinnati
Cincinnati, OH

WILEY-INTERSCIENCE

A JOHN WILEY & SONS, INC., PUBLICATION

New York • Chichester • Weinheim • Brisbane • Singapore • Toronto

TD884.5
.A249
2001

This book is printed on acid-free paper. ♾

Copyright © 2001 by John Wiley and Sons, Inc. All rights reserved.

Published simultaneously in Canada.

No part of this publication may be reproduced, stored in a retrieval system or transmitted in any form or by any means, electronic, mechanical, photocopying, recording, scanning or otherwise, except as permitted under Sections 107 or 108 of the 1976 United States Copyright Act, without either the prior written permission of the Publisher, or authorization through payment of the appropriate per-copy fee to the Copyright Clearance Center, 222 Rosewood Drive, Danvers, MA 01923, (978) 750-8400, fax (978) 750-4744. Requests to the Publisher for permission should be addressed to the Permissions Department, John Wiley & Sons, Inc., 605 Third Avenue, New York, NY 10158-0012, (212) 850-6011, fax (212) 850-6008, E-Mail: PERMREQ@WILEY.COM.

For ordering and customer service, call 1-800-CALL-WILEY.

Library of Congress Cataloging-in-Publication Data:

Aerosol measurement : principles, techniques, and applications / [edited] by Paul A. Baron and Klaus Willeke.—2nd ed.

p. cm.

Includes index.

ISBN 0-471-35636-0 (cloth)

1. Aerosols—Measurement. 2. Air—Pollution—Measurement. I. Baron, Paul A., 1944– II. Willeke, Klaus.

TD884.5 .A33 2001

628.5'3'0287–dc21 2001017845

Printed in the United States of America.

10 9 8 7 6 5 4 3 2 1